Linköping University | Department of Management and Engineering
Master's thesis, 30 ECTS | Mechanical Engineering
Spring 2024 | LIU-IEI-TEK-A–24/04802–SE

Predictions of Vibrations in Aircraft Structure

Random Response Analysis of a Conceptual Aircraft Subject to Sound Pressure from Flow Over an Internal Weapon Bay

William Larsson
Johan Nordahl

Industrial supervisors
Johan Hammar
Peter Davidsson

Examinator
Peter Schmidt

Academic Supervisor
Jonas Stålhand

Linköping University
SE-581 83 Linköping, Sweden
+46 013 28 10 00, www.liu.se

Abstract

Vibration is a vital field in physics, especially within the aeronautical industry, where precise vibration prediction is crucial to prevent structural failures and equipment damage. During the conceptual phase of aircraft design, the prediction of the vibrational environment is highly valuable. This thesis examines the vibrational environment in an aircraft structure subjected to cavity oscillations caused by an internal weapon bay. The study uses the ESDU 18011 standard to model a continuous non-deterministic excitation resulting from these oscillations. The aims are to investigate the necessary model fidelity to accurately capture the vibrational environment in the frequency range, to model and install damping mats to investigate the influence on the dynamical behaviour, and to examine the effect of equipment mounting on local vibration responses. The methodology begins with designing the downstream wall of the internal weapon bay to withstand fatigue and resonance due to increased sound pressure. This redesigned wall is then incorporated into the aircraft structure. Structural fidelity is assessed by implementing reinforcements, point masses, and fuel. The effects of damping mats on the vibrational environment are evaluated by modelling and mounting them. Furthermore, the study analyses the local impact of the mounting of the equipment on vibrations. The results show that high model fidelity is crucial near the internal weapon bay, a dense mesh is required to accurately capture the wave propagation for higher frequencies, damping mats influence the dynamic behaviour, and equipment mounting substantially decreases local vibrational amplitudes.

Keywords: Vibrational response, random vibrations, random response, acoustics, cavity oscillations, finite element analysis, damping

Acknowledgement

We would like to express our deepest gratitude to our supervisors at SAAB Aeronautics, Peter Davidsson and Johan Hammar, for their enthusiastic involvement in this work. Their knowledge and expertise were instrumental to this research, and it would not have been possible without their support. We are also thankful to everyone at the Department of Environmental Engineering at SAAB for their assistance whenever we needed it.

We would like to acknowledge the help received from our academic supervisor, Jonas Stålhand, and our examiner, Peter Schmidt, for their invaluable advice and guidance.

Linköping 2024

William Larsson
Johan Nordahl

Abbreviation

ESDU	-	Engineering Sciences Data Unit
PSD	-	Power Spectral Density
RMS	-	Root Mean Square
IWB	-	Internal Weapon Bay
FEA	-	Finite Element Analysis
dofs	-	Degrees of freedom

Glossary

Baseline model	-	Generic aircraft model. Reinforcements, point masses, and fuel included.
Power spectral density	-	Indicates where the concentration of signal is located over the frequency span.
Root mean square	-	Integral of the Power spectral density.
Frequency-response function	-	Relation between the respons and excitation.
Hypermesh	-	FEA pre-processor.
Optistruct	-	Solver.
Matlab	-	Software for mathematical and technical calculations.
ESDU 18011	-	Standard for cavity oscillations
ESDU FAT E.07.01	-	Handbook with experimental fatigue data for aluminium.
Skin field	-	Skin field on the frame web. Plate between reinforcements.
Loss factor	-	Ratio of energy dissipated. compared to the undamped peak.

Contents

1 Introduction **1**
- 1.1 Background . . . 1
- 1.2 Purpose and aim . . . 1
- 1.3 Problem statement . . . 2
- 1.4 Delimitation . . . 2
- 1.5 Method . . . 2

2 Theory **4**
- 2.1 Cavity oscillations . . . 4
- 2.2 Random vibrations . . . 5
  - 2.2.1 Power Spectral Density . . . 7
  - 2.2.2 Root mean square . . . 9
  - 2.2.3 Frequency-response function . . . 9
  - 2.2.4 Random response analysis . . . 10
  - 2.2.5 Calculating response based on the frequency-response function for mass mounting and external pressure field . . . 11
- 2.3 Damping . . . 11
- 2.4 ESDU standards . . . 12
  - 2.4.1 ESDU 18011 . . . 12
  - 2.4.2 ESDU FAT E.07.01 . . . 12

3 Method **13**
- 3.1 Design of downstream wall . . . 13
  - 3.1.1 Excitation . . . 13
  - 3.1.2 Model requirements . . . 13
  - 3.1.3 Model setup . . . 15
- 3.2 Aircraft structure . . . 16
  - 3.2.1 Geometry . . . 16
  - 3.2.2 Structural components of the aircraft . . . 18
  - 3.2.3 Boundary conditions and mesh . . . 19
  - 3.2.4 Material data and structural thickness . . . 19
  - 3.2.5 Modal analysis . . . 19
  - 3.2.6 Point masses . . . 19
  - 3.2.7 Excitation . . . 20
  - 3.2.8 Modelling fuel . . . 21
  - 3.2.9 Specification requirement . . . 22
  - 3.2.10 Vibrational response in the frequency range 10-2000 Hz . . . 22
  - 3.2.11 Modelling damping mats . . . 24
- 3.3 Impact of equipment mounting position . . . 27
- 3.4 Validation . . . 29

4 Results and Discussion **30**
4.1 PSD excitation . . . 30
4.2 Designing the downstream wall . . . 30
4.3 Vibration environment of aircraft structure . . . 35
4.3.1 Modal analysis . . . 35
4.3.2 Vibrational response in the frequency range 10-2000 Hz . . . 36
4.3.3 Modelling damping mats . . . 41
4.4 Impact of equipment mounting position . . . 50
4.5 Validation . . . 53

5 Conclusion **55**

6 Further work **56**

A Random Response analysis **59**

B Fundamental Finite elements **59**
B.1 1D elements . . . 59
B.1.1 bar2 elements . . . 60
B.2 Shell elements . . . 60
B.3 Solid elements . . . 61
B.4 CONM2 elements . . . 62
B.5 RBE3 elements . . . 62
B.6 MFLUID . . . 63
B.6.1 Theory and Method . . . 63
B.6.2 Comparison with and without MFLUID . . . 63

1 Introduction

This master's thesis was conducted at the Department of Environmental Engineering and Thermal Analysis at Saab Aeronautics in Linköping, Sweden. Saab, established in 1937 with a focus on developing and producing combat aircraft, has since expanded its operations to various sectors [1]. In addition to its aeronautical division, known for developing and producing aircraft such as Gripen, Saab also includes Dynamics, which specialises in ground combat weaponry such as Carl-Gustaf and NLAW, Surveillance, responsible for GlobalEye AEW& C, and Kockums, which is involved in manufacturing naval systems such as submarines and surface vessels [2].

The department of Environmental engineering and thermal analysis is primarily concerned with ensuring that the aircraft and its equipment will function reliably in the environment they are exposed to. All the way from the cold in northern Sweden down to the warmth in South America.

1.1 Background

The vibrational environment in an aircraft is generated by multiple sources. The vibration may originate from turbulent boundary layer around the aircraft, disturbances in the airflow leading to high dynamical pressure levels, as well as internal sources such as rotating equipment, for instance the gearbox or the engine. Regardless of the source, the impact needs to be predicted and validated. Currently this is done experimentally by measuring the vibration on the aircraft, and the connections between the source and the response are vague.

One such source is generated by flow over open cavities. Flow over open cavities such as landing gear bays and internal weapon bays generates energetic pressure fluctuations that will interact with the structure. This, is primarily a problem for the internal weapon bay since the landing gear is only extended at low Mach numbers. These pressure fluctuations will give rise to static and dynamic deformations causing high vibration levels which may have sever implications on equipment. [3]

To be able to predict the the impact of the cavity the source need to be described as well the vibrational response in the structure. A generic CAD-model of an aircraft including a Internal Weapons Bay (IWB) is available. However, this needs to be updated in order to be suitable for use in dynamic analysis. For example, the stiffeners of the frames need to be included.

1.2 Purpose and aim

The purpose of the thesis is to contribute to the understanding of the vibrational response of an aircraft structure due to excitation from cavity oscillations and to be able to accurately predict the vibration in the frequency range. The primary focus is to create a FE model suitable for dynamic analysis from a generic aircraft model. The influence on dynamic behaviour from damping mats and attachment of equipment is also implemented and analysed.

1.3 Problem statement

- How should the generic CAD-model be updated to have a viable dynamic behaviour in the frequency range of interest.
- How well does the model capture the dynamic behaviour in the frequency range of interest.
- How do damping mats influence the vibrational response.
- How does the instalment position and mass of equipment influence the vibrational response.

1.4 Delimitation

The softwares used in this project is mainly Matlab for analytical calculations and post-processing, Hypermesh for FE modelling and Optistruct as a solver. The work is limited to vibrational analysis. The load case is based on well-known standards, and no aerodynamic or thermal analysis is performed.

1.5 Method

The primary focus of this thesis is to conduct a random response analysis and investigate the resulting vibrational environment on a generic aircraft structure.

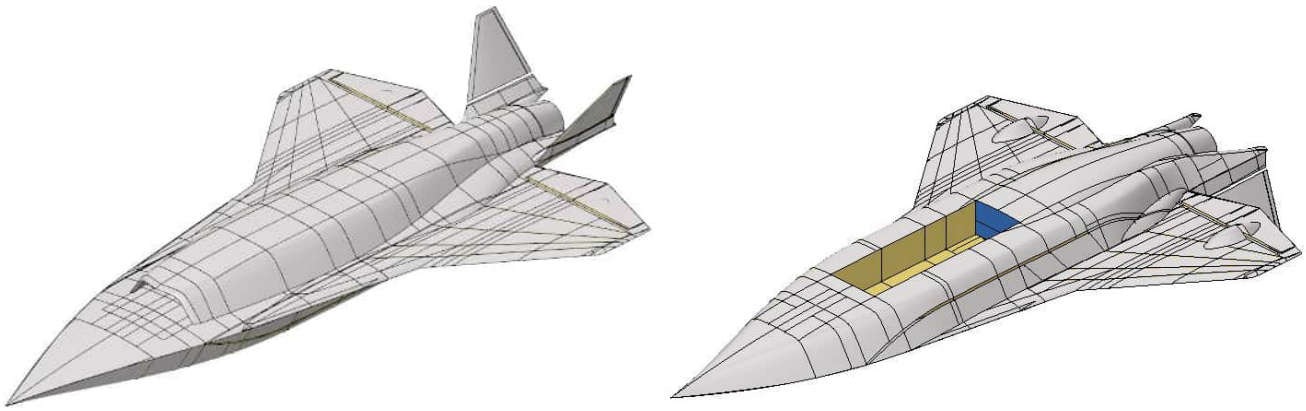

Figure 1: Generic aircraft structure

Figure 1 shows the generic aircraft structure both from above and below. The highlighted blue structural component represents the downstream wall of the internal weapon bay, exposed to the highest level of sound pressure levels due to flow over an open cavity. The work is divided into two parts. Part one consists of designing the downstream wall to avoid fatigue and resonance due to the increase in sound pressure. Part two consists of incorporating the updated design of the downstream wall and updating the CAD model to have a reasonable behaviour in the frequency range of interest then performing a random response analysis to investigate the vibrational response and propagation.

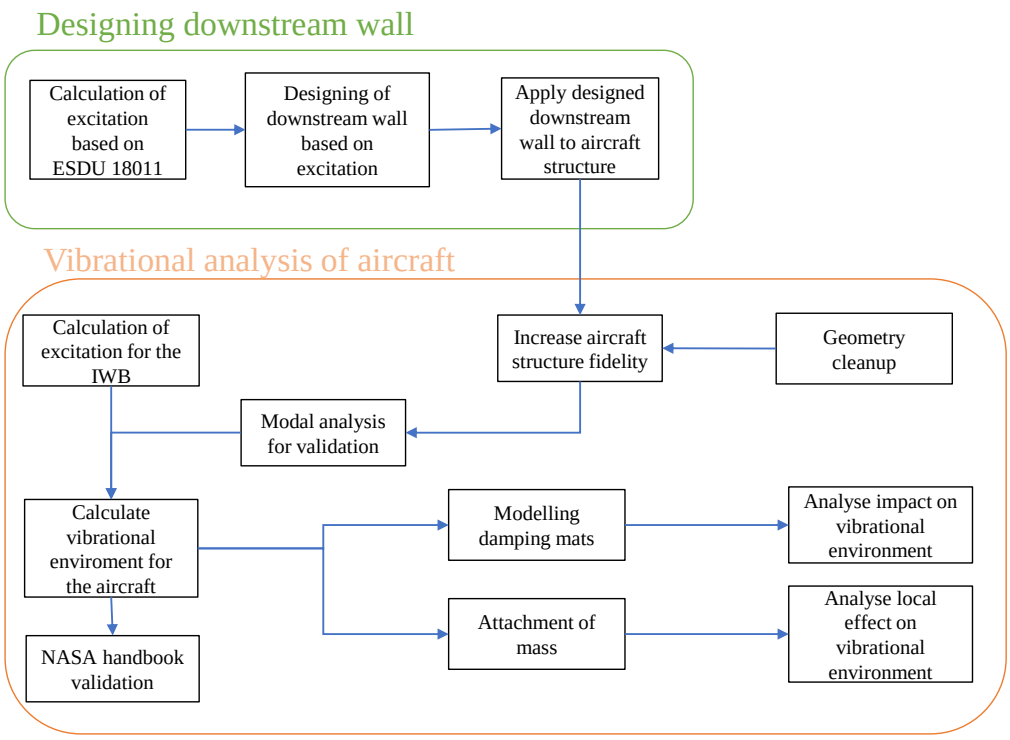

Figure 2: Overview of the methodology used in this work. The thesis is divided into two parts, first the downstream wall is designed to withstand both fatigue and resonance. In the second part the design is implemented and work is conducted to create a suitable model for a random response analysis of an aircraft. The model is then analysed for the effects on vibrational behaviour.

Figure 2 provides an overview of the work conducted in the thesis.

2 Theory

2.1 Cavity oscillations

The cavity problem is a well-studied case in fluid mechanics and aerodynamics. The two most used examples of cavities for a combat aircraft are internal weapon bays and landing gears. The difference between flow over a landing gear cavity and an internal weapon bay is when the two systems are used. Landing gears are operated at low Mach numbers while the weapon bays are intended to be used at a larger span of Mach numbers, spanning from subsonic up to super sonic speeds. The cavity flow is divided into two characters, open cavity flow and closed cavity flow. [3]

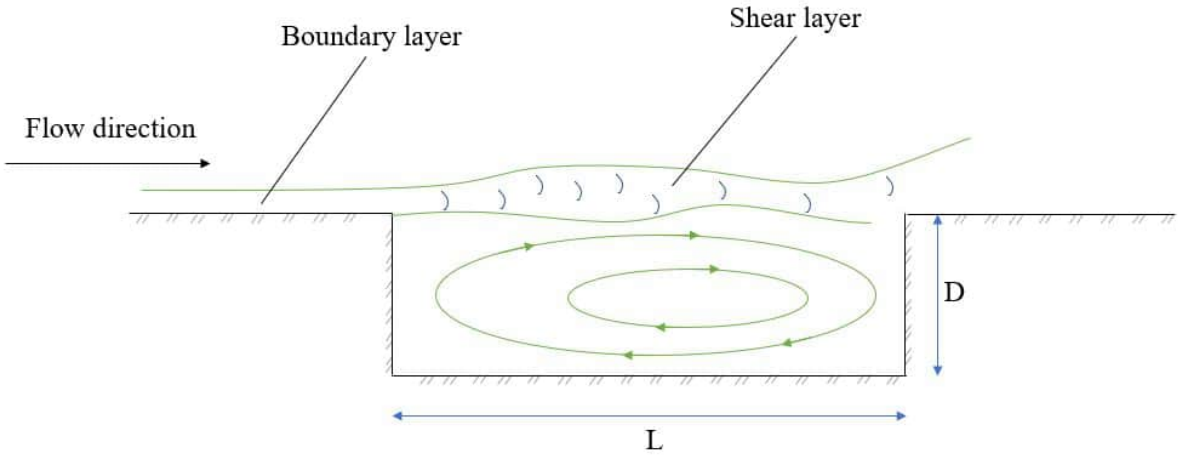

Figure 3: Open cavity flow. The boundary layer can be either laminar or turbulent. Over the cavity a shear layer with turbulent flow is developed. Inside the cavity the flow is circulating.

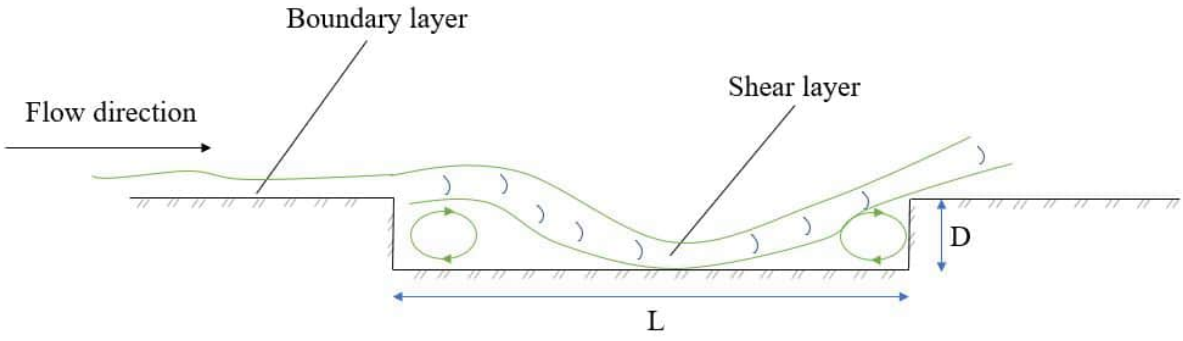

Figure 4: Closed cavity flow. The boundary layer can be either laminar or turbulent. Over the cavity a shear layer with turbulent flow is formed and attaches to the floor of the cavity. Inside the cavity circulation zones are formed in connection with the steps.

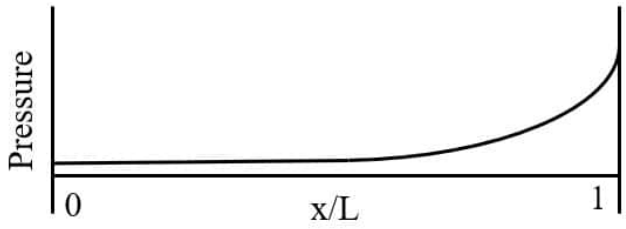

Figure 5: A schematic pressure distribution lengthwise inside of the cavity based on the ESDU18011 model for open cavity flow. x is the coordinate along the cavity and L is the cavity length [4].

The question of whether the flow over a cavity is considered open or closed depends on the Mach number and length-to-depth ratio (L/D ratio in Figures 3 and 4). If L/D is between 9-15 the cavity is considered closed and if L/D is less than a value between 6-8 the cavity is considered open. If L/D is between 8-9, the cavity flow is transitional. A shallow cavity tends to be closed because the flow attaches to the floor of the cavity, while a deep cavity tends to be open. [4]

In Figures 3 and 4, two layers of flow can be seen, namely boundary layer and shear layer. The boundary layer is a thin layer of flow next to the surface. The velocity is zero at the surface and increases to the free-stream velocity at the top of the layer. When the flow reaches the leading edge of the cavity, it will separate, creating a turbulent region over the cavity known as the shear layer. The shear layer consists of vortices with different velocities, thus creating pressure fluctuations. When the vortices hit the downstream wall, an acoustic wave is generated. The acoustic wave travels upstream in the cavity and affects the shear layer at the leading edge causing more unstable vortices at the leading edge of the cavity. This cycle repeats itself with an increase in the acoustic wave amplitude for small frequency bands when the phase of the waves coincide. The phenomenon is called flow-induced resonance, and the resonant modes are referred to as Rossiter modes. The levels of energy from aeroacoustic waves are measured in terms of the sound-pressure level and depend on the free-stream flow and the dimensions of the cavity. [5, 6]

Figure 5 shows a schematic pressure distribution along the cavity for an open cavity. The sound pressure levels increases exponentially from the upstream wall to the downstream wall. [4]

2.2 Random vibrations

To accurately analyse mechanical and structural systems that are subjected to realistic dynamic environments, consideration must be taken with respect to the randomness of parameters and excitation. Parameters can, for instance, have random variations in stiffness, mass, or damping due to temperature differences while excitations can be generated due to some random mechanism. This can be treated by using random vibrations which allows for a statistical description of the randomness to both the input and the response. [7]

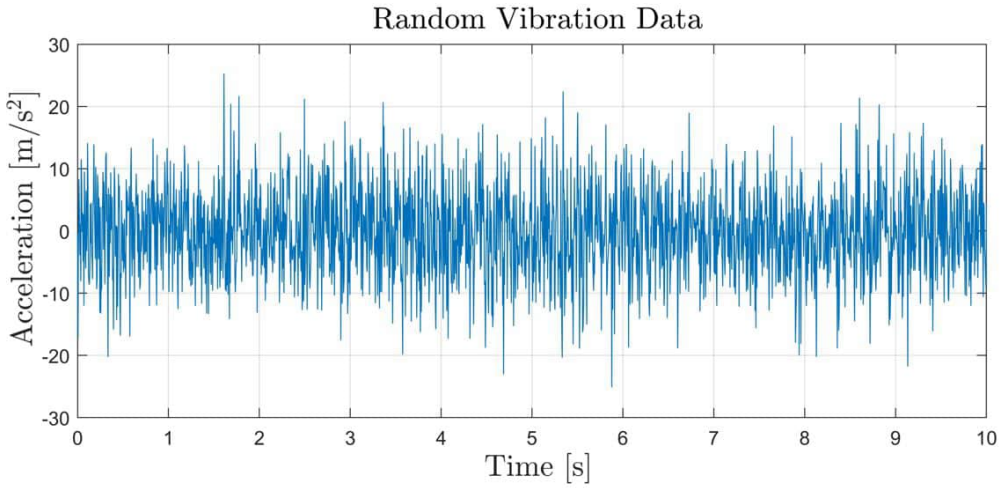

Figure 6: An example of random vibration signal, $X(t)$, from an accelerometer.

Measuring a random signal $X(t)$, as showcased in Figure 6, at different times will result in values that behave according to some probability distribution which, in turn, depends on the nature of the random process. Generally, the Gaussian, or normal, distribution is considered in random vibration. Activating the random process generates one sample of the signal. Generating multiple samples leads to a set of samples which is called an ensemble. Averaging one sample over time leads to the time average of that history, known as the sample mean. Averaging of all data from the ensemble at a specific time leads to the ensemble average at that time, which is known as the expected value of the signal and is denoted $E|X(t)|$. In computations involving random signals, the *ergodic hypothesis* is frequently utilised. This hypothesis suggests that for a sufficiently long single sample $x(t)$ from the random process $X(t)$, the time mean of $x(t)$ will converge to the expected value of the random process. [8]

Given the probability density function, which describes the probability distribution, of the random process $X(t)$ given by a function p, the statistics of the ensemble can be calculated at time t. The mean is equal to the expected value and given by,

$$\mu_x(t) = E[X(t)] = \int_{-\infty}^{+\infty} xp(x)dx, \tag{1}$$

as well as the variance,

$$\sigma_x^2(t) = E[X(t) - \mu_x(t)^2] = \int_{-\infty}^{+\infty} [x - \mu_x(t)]p(x)dx. \tag{2}$$

A signal is considered stationary if for a random signal $X(t)$, the joint statistical properties of the signal at two different time points t_1 and t_2 is independent of t and instead dependent on the time difference $(t_2 - t_1)$. The correlation of the process with itself is then given by the stationary auto-correlation function,

$$R_X(\tau) = R_x(t, t+\tau) = E[X(t)X(t+\tau)], \tag{3}$$

where $\tau = t_2 - t_1$ and is called the lag.

The cross correlation is concerned with the correlation between two random signals for instance $X(t)$ and $Y(t)$ if these are considered stationary R_{XY} is given by,

$$R_{XY}(\tau) = E[X(t)Y(t+\tau)]. \tag{4}$$

Stationary vibrations are more useful to examine in the frequency domain compared to the time domain. Through the Power Spectral Density (PSD) of the random signal, it is possible to estimate the amount of energy contained in the frequency range. [8]

2.2.1 Power Spectral Density

Power Spectral Density is used to describe the power as a function of frequency for random signals. One example of a random signal is wind acting on a building. Thus, a PSD graph tells where the signal power is concentrated over the chosen frequency range. [9]

A signal is usually described in the time domain and therefore needs to be transformed to the frequency domain. This can be done by using the fast Fourier transformation. [9]

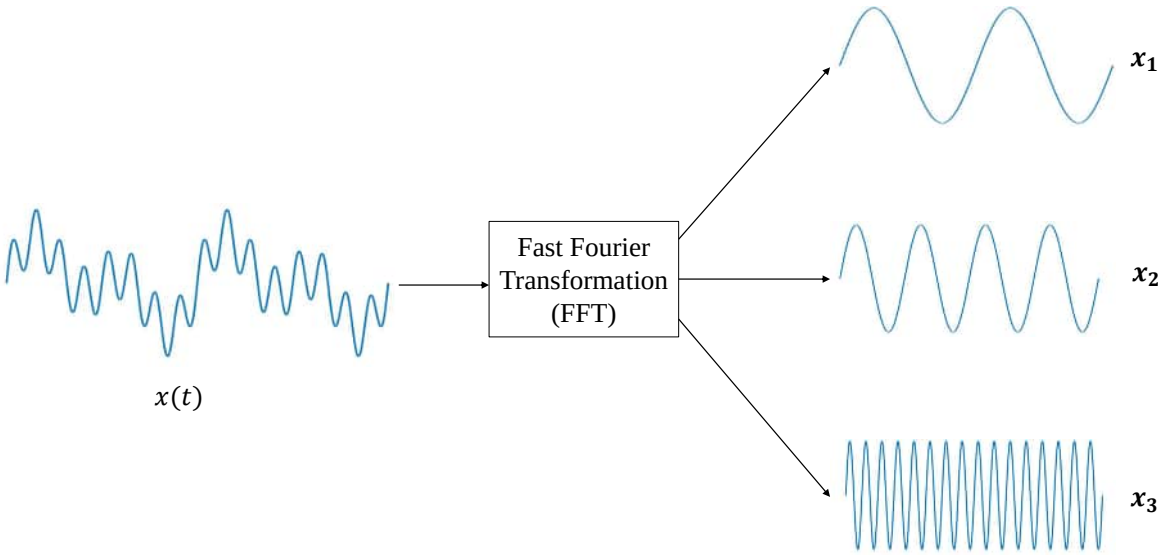

Figure 7: Decomposition of the complex vibration, $x(t)$, in three components $\mathbf{x_1}, \mathbf{x_2}$ and $\mathbf{x_3}$

Figure 7 shows how the Fourier transformation decomposes a complex vibration into multiple components.

By performing a Fourier transform of the auto-correlation function, the the power spectral density function is obtained,

$$S_X(f) = \int_{-\infty}^{\infty} R_X(\tau) e^{-i2\pi f\tau} d\tau, \tag{5}$$

for the random process $X(t)$, where f is the frequency. The same holds for the cross-spectral density between $X(t)$ and $Y(t)$,

$$S_{XY}(f) = \int_{-\infty}^{\infty} R_{XY}(\tau) e^{-i2\pi f\tau} d\tau. \tag{6}$$

Due to symmetry, the PSD function has the property

$$S_X(-f) = S_X(f). \tag{7}$$

Using Equation (7), the power spectral density functions can be written, (5) and (6) can be written [10],

$$\begin{cases} S_X(f) = 2\int_0^{\infty} R_X(\tau) e^{-i2\pi f\tau} d\tau & f > 0, \\ S_{XY}(f) = 2\int_0^{\infty} R_{XY}(\tau) e^{-i2\pi f\tau} d\tau & f > 0. \end{cases} \tag{8}$$

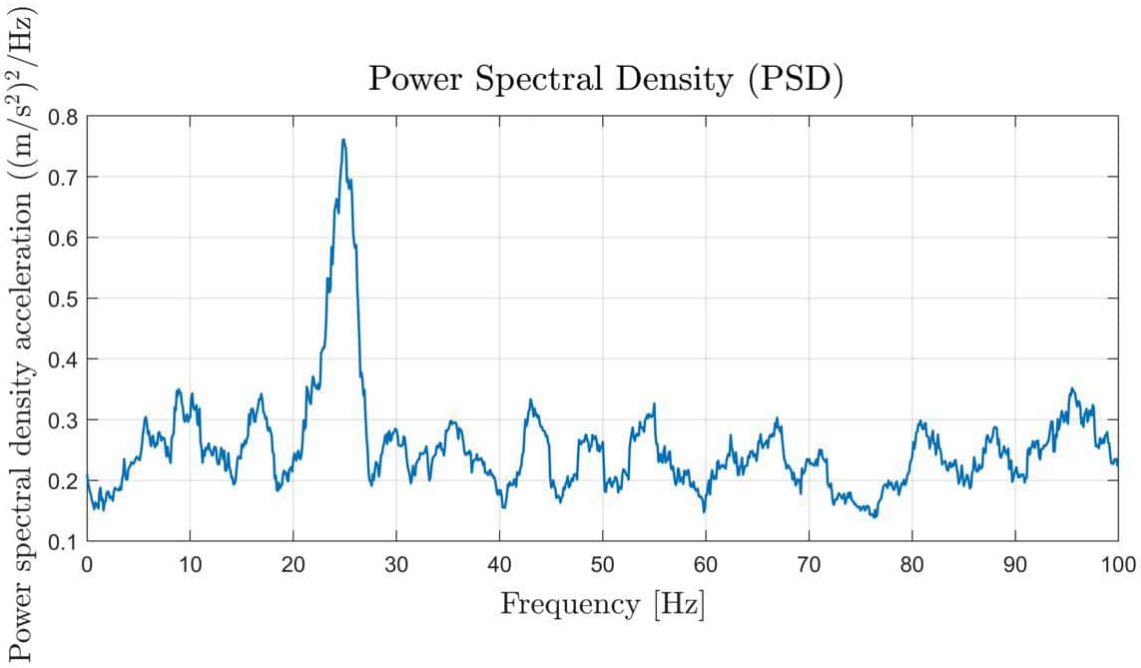

Figure 8: PSD curve from the data in Figure 6. From the figure it is clear that the energy content is concentrated around 25 Hz.

Figure 8 shows a PSD curve. The result states that there is a high concentration of signal power at around 25 Hz. The unit for PSD is (measured unit)^2/Hz, thus if the acceleration in m/s^2 is analysed, the unit for the PSD acceleration is (m/s^2)^2/Hz. Vibration is also commonly measured relative to gravity in engineering applications resulting in accelerations specified in terms of g and PSD accelerations in terms of g^2/Hz. To covert the result from (m/s^2)^2/Hz to g^2/Hz, the result in (m/s^2)^2/Hz is divided with g^2.

2.2.2 Root mean square

The expected value of the random variable X squared, $E[X^2]$ is known as the mean-square value. If the mean of X is zero the mean-square is equal to the variance and the root-mean square (RMS) is equal to the standard deviation. The mean square can also be derived from the area under the power spectral density curve if the mean is assumed to be zero. By taking the square root of the mean value, the standard deviation or RMS is obtained,

$$\sigma_X = \sqrt{R_X(0)} = \sqrt{\int_0^\infty S_X(f)df}. \tag{9}$$

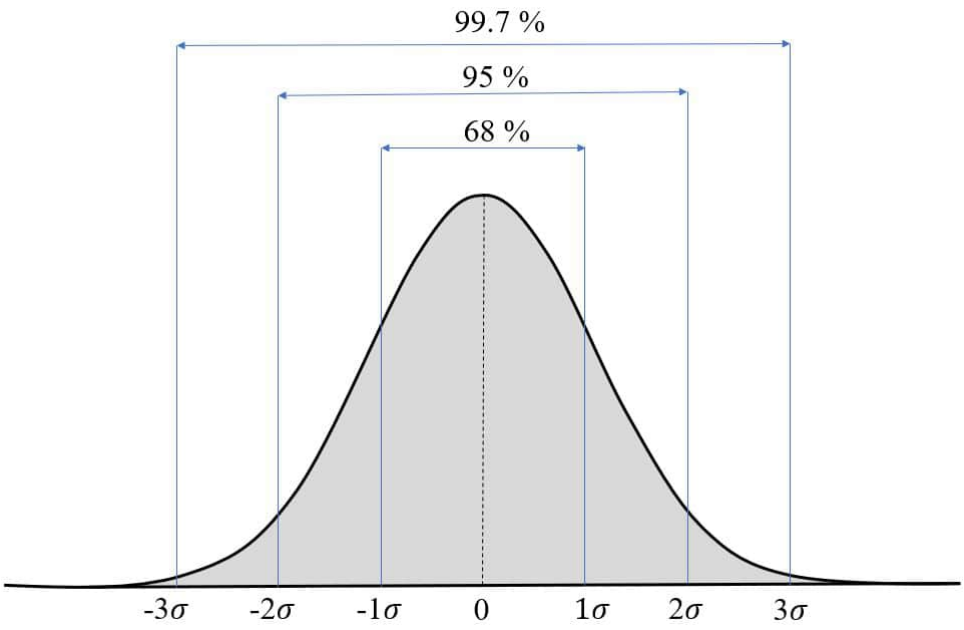

Figure 9: Gaussian distribution curve with standard deviations.

Considering a Gaussian distribution visible in Figure 9, the responding RMS result fall within ± one standard deviation of the mean, approximately 68% of the time. This highlights the statistical sense of the results which the random-response analysis provides. To ensure a conservative measure, the RMS value is multiplied by three, adhering to the three-sigma design criterion, which captures values that will be exceeded only 0.3% of the time. This process is often used to account for variability and ensure that the design is robust enough to satisfy requirements under extreme conditions. [8]

2.2.3 Frequency-response function

To characterise the structural response due to excitation in the frequency domain, a frequency-response function (FRF) is established. The function forms a relationship between the response of the system and the input excitation:

$$H(f) = \frac{Y(f)}{X(f)}, \tag{10}$$

where $Y(f)$ is the response and $X(f)$ is the excitation [10]. The frequency-response function is usually characterised in one of two ways depending on the analysis (modal-frequency-response analysis or direct-frequency-response analysis). The modal frequency-response analysis uncouples the equations of motion and uses the normal modes to compute the response. Contrasting, the direct method computes the response by directly solving the equation of motions at discrete frequencies. The normal-mode method is generally less computationally expensive. At high-frequency excitation's, however, the direct method proves more efficient due to the amount of modes needed to be extracted in the normal-mode method [11].

2.2.4 Random response analysis

A random response analysis is used to predict the response of a system subjected to a non-deterministic, continuous excitation. Two examples of excitations are turbulence and wind. The random response of the structure is calculated from the frequency response and the input PSD. The output of the analysis becomes a PSD.

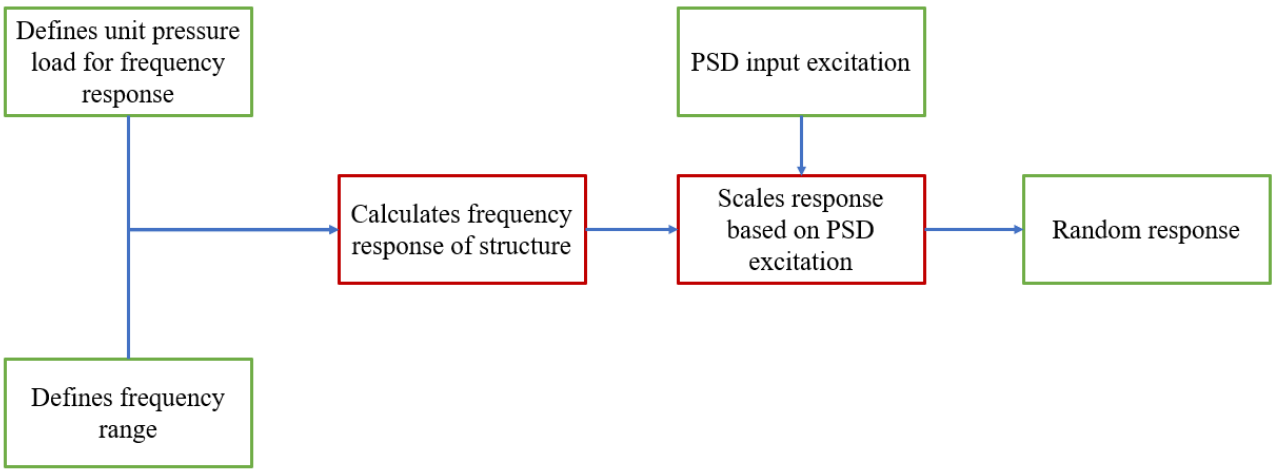

Figure 10: Set-up of a random response analysis.

Figure 10 shows how a random response analysis is set-up and solved in a FE solver. The response is also random and defined by a PSD,

$$S_y(f) = |H(f)|^2 S_x(f), \tag{11}$$

where S_x is the input PSD and $|H(f)|$ is the magnitude of the complex frequency response for single degree of freedom [10].

2.2.5 Calculating response based on the frequency-response function for mass mounting and external pressure field

To reduce the computational time needed to calculate the response of the structure due to different mass values the frequency-response function (FRF) of the structure can be used. From the formula of forced undamped vibrations:

$$\mathbf{M}\ddot{\mathbf{d}} + \mathbf{K}\mathbf{d} = \mathbf{F_{tot}}. \tag{12}$$

$\mathbf{M}$ is the mass matrix, $\mathbf{K}$ is the stiffness matrix, $\mathbf{F}_{tot}$ is force matrix and $\mathbf{d}$ is the displacement vector. Assuming,

$$\mathbf{d} = \mathbf{d}_0 \sin \omega t, \tag{13}$$

where $\mathbf{d}_0$ is a constant vector, ω is the angular velocity, and t denotes time. Differentiating the displacement vector twice and inserting it into Equation (12) gives

$$(-\omega^2\mathbf{M} + \mathbf{K})\mathbf{d} = \mathbf{F}_{tot}. \tag{14}$$

Differentiate the displacement vector $\mathbf{d}$ twice to get the acceleration vector, $\mathbf{a}$.

$$(\mathbf{M} - \frac{1}{\omega^2}\mathbf{K})\mathbf{a} = \mathbf{F}_{tot}. \tag{15}$$

Where ω^2 is the eigenvalue of the structure, and $\mathbf{a}$ is the acceleration response. The matrix $(\mathbf{M} - \frac{1}{\omega^2}\mathbf{K})$ is known as dynamic stiffness and is denoted $\mathbf{D}$. Taking $\mathbf{D}^{-1}$ give the FRF matrix $\mathbf{H}$, and Equation (15)gives,

$$\mathbf{a} = \mathbf{H}\mathbf{F}_{tot}, \tag{16}$$

where $\mathbf{F}_{tot}$ consists of the force from the external pressure as well as the force from the mass (from equipment) acting on the surface. The acceleration for a point, in which the mass is mounted can be written,

$$\mathbf{a} = \mathbf{a}^{ext} + \mathbf{H}\mathbf{F}_{masspoint}, \tag{17}$$

where $\mathbf{a}^{ext}$ is the acceleration generated from the external pressure field, $\mathbf{F}_{masspoint}$ is the force corresponding to the mounted mass and is calculated through,

$$\mathbf{F}_{masspoint} = \mathbf{G}(\mathbf{I} - \mathbf{H}\mathbf{G})^{-1}\mathbf{a}^{ext}, \tag{18}$$

where $\mathbf{G}$ is the analysed mass matrix of the equipment in the mass mounting degrees of freedoms (dofs) and where Equation (18) is used to obtain the acceleration response due to added mass in the masspoint. By using the responding acceleration in Equation (10) to obtain the new FRF, Equation (11) can be used to calculate the PSD acceleration.

2.3 Damping

Damping is a process where mechanical energy is transformed into heat energy, leading to dissipation. This mechanism is present in some form in all kinds of structures but is generally divided into three different categories. [12]

Internal *material damping* refers to the dissipation of mechanical energy originating from processes within the material itself, such as the movement of dislocations or variations in local temperature. A type of material frequently utilised for its superior internal material damping properties is viscoelastic material which transforms mechanical energy into heat as a result of internal friction. The occurrence of *structural damping* can be attributed to the dissipation of mechanical energy that arises from friction, which is a consequence of the relative movement between interacting structural components such as joints or supports.

Through fluid-structure interactions mechanical energy can also be dissipated due to the dynamic interaction between the fluid and the structure, this is known as *fluid damping*.

An aircraft is generally made of metals with little internal damping, and, in order to reduce the vibrational amplitude, damping mats are added to surfaces that are exposed to high vibrational amplitudes. This method of reducing vibrations is commonly used in the aeronautical industry. By combining the damping layer on a surface with a thin layer of stiff metal, the mat absorbs energy by forcing the rubber to shear. This is called constrained-layer damping [10]. Rubber is considered one of the best materials to have as a damping layer because it can be manufactured with high damping-coefficient properties and still be resilient to low levels of creep [13]. The ratio of energy that is dissipated compared to the undamped peak is referred to as the loss factor [12].

2.4 ESDU standards

2.4.1 ESDU 18011

ESDU 18011 is a standard that describes how to model cavity oscillations. It also accounts for how the flow over an open cavity creates intense sound and thus sound pressures that affects the cavity. The sound pressure level is scaled based on the longitudinal location in the cavity that is investigated. The sound pressure levels are given in one-third-octave bands. [4]

2.4.2 ESDU FAT E.07.01

ESDU FAT E.07.01 is a handbook with around 3500 amplitude tests to determine the S-N curve (Wöhler curve) for aluminium alloys in bending. This data is used to analyse the FEA stress against fatigue. [14]

3 Method

3.1 Design of downstream wall

The first phase involves designing the downstream wall due to its exposure to elevated sound pressure upon opening the IWB. It must consequently be designed to prevent failure. This was done by examining the RMS response and comparing the result to the three-sigma design criterion for different configurations of the downstream wall. Additionally the natural frequency was determined to ensure that the frequency of the excitation does not coincide with the frequency of the three lowest Rossiter modes of the cavity. The downstream wall was analysed through an iterative process where the pattern, element-type, and dimension of the reinforcement as well as the boundary condition were investigated.

3.1.1 Excitation

The airflow over the cavity will result in high sound pressure levels, which will act as the excitation source for the downstream wall. The sound pressure levels as a function of frequency are calculated using the standard ESDU18011 in one-third-octave bands. The levels depend on the Mach number, altitude, and the length-to-depth ratio of the cavity. The spectrum sound pressure levels are then converted into power spectral density to be used as input into FEM. The flight parameters and dimensions of the IWB are shown in Table 1.

Table 1: Parameters used for the calculation of the excitation.

Mach	1.2
Altitude	3000 m
Length	3.15 m
Depth	0.57 m
L/D	5.5

Since the value for L/D is below 6-8 the cavity flow is in this case considered as open and the pressure distribution follows Figure 5, where the pressure will increase exponentially from the upstream wall to the downstream wall.

3.1.2 Model requirements

The geometry of the downstream wall is pre-defined with a length of 950 mm, a width of 600 mm, and a thickness of 2.5 mm. Reinforcements are added to increase its stiffness. The material for both the downstream wall and reinforcements is aluminum with material data according to Table 2.

Table 2: Aluminum material data.

Young's modulus	70 GPa
Density	2800 kg/m^3
Poisson's ratio	0.3
Structural damping	10%

It is assumed as a design criterion that the third Rossiter mode must be lower than the first natural frequency of the downstream wall to avoid resonance. A safety factor of 50% is implemented to account for uncertainties,

$$f_n \geq 1,5 f_{3,Ros}, \tag{19}$$

where f_n refers to the natural frequency of the downstream wall and $f_{3,Ros}$ refers to the third Rossiter mode.

To further ensure that the downstream wall is correctly designed for the sound pressure excitation concerning fatigue, the RMS stress is compared to the endurance data of aluminium alloys in bending. The three-sigma design criterion is used to ensure that fatigue will be avoided 99.7% of the time. The fatigue limit for the material aluminium 7075 is 90 MPa for a life above 10^8 cycles based on data from experiments in ESDU FAT E.07.01. Based on the three sigma design criterion fatigue is therefore avoided if the RMS stress (one standard deviation) is at or below 30 MPa. [14].

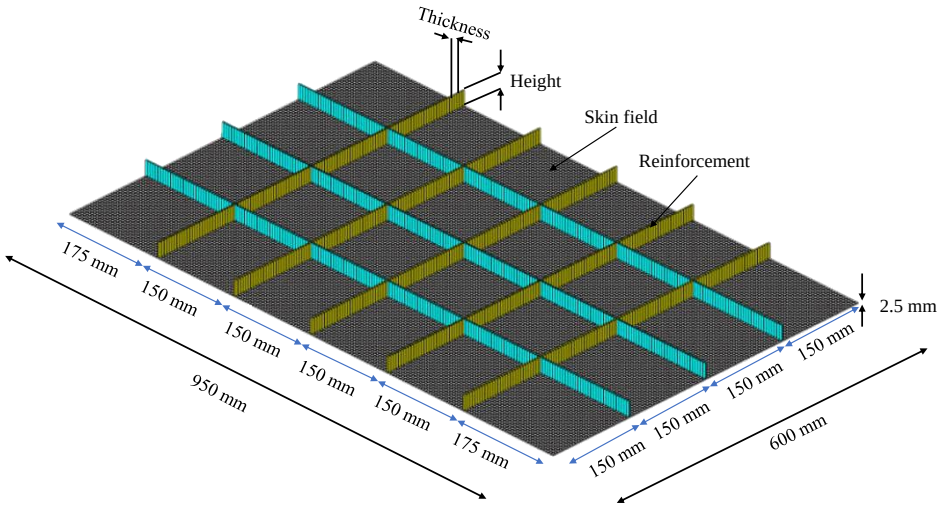

Figure 11: Downstream wall model with measurements and terminology indications used in the thesis. 'Skin field on the frame web' is abbreviated to 'Skin field.'

Figure 11 shows the downstream wall and its terminology. Skin field on the frame web is referred to as the skin field in the rest of the thesis.

Designing the reinforcement was an iterative process to fulfil the three-sigma-design criterion and the inequality in Equation 19. The design of the reinforcement pattern was decided based on expertise, and to find some balance between added mass from the reinforcements and added stiffness. The final reinforcement pattern was designed with 150x150 mm spacing between each reinforcement, resulting in a 5x3 grid pattern and a residual 50 mm evenly distributed on both sides,

leading to 175 mm from the outer reinforcements to each edge. Figure 11 shows the final reinforcement pattern for the downstream wall. Two different reinforcement dimensions were analysed for comparison. The two dimensions are: a height of 25 mm, a thickness of 2.5 mm and a height of 22 mm, with a thickness of 2.2 mm.

Both the downstream wall and the reinforcements are modelled as first order elements with an element size of 5 mm.

The model is fixed around the edge, thus no displacement in either axis direction or rotation around the axes is allowed. These boundary conditions are intended to resemble how the downstream wall is connected in the aircraft.

3.1.3 Model setup

A modal analysis of the model is conducted, and the first natural frequency of the structure is analysed against the inequality in Equation (19) to avoid resonance.

A random response analysis is then performed on the downstream wall. The sound pressure excitation on the downstream wall is found from the standard ESDU18011 as described in chapter 3.1.1. The downstream wall is excited by a uniform pressure across the entire downstream wall. The response is then scaled by the input PSD. The response of the downstream wall in form of PSD and RMS stress is then analysed to make sure that it can withstand the applied load without leading to fatigue.

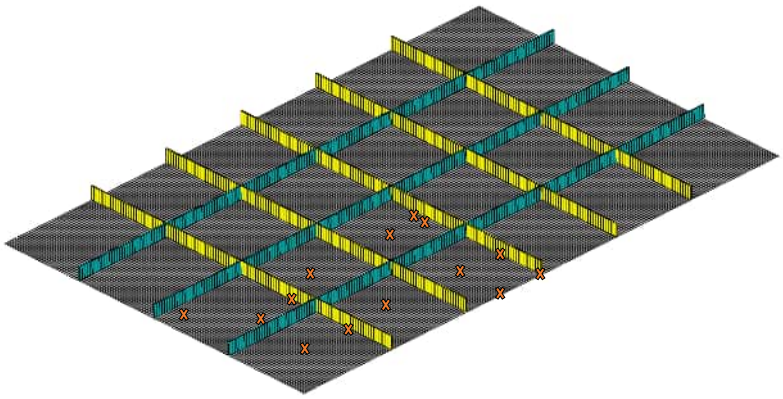

Figure 12: Element location used to analyse the downstream wall.

Figure 12 illustrates the positioning of elements for the analysis of the downstream wall. The elements were chosen to capture the whole range of responses. The results are symmetrical across all four quadrants, therefore, examining elements in a single quadrant is considered sufficient.

3.2 Aircraft structure

3.2.1 Geometry

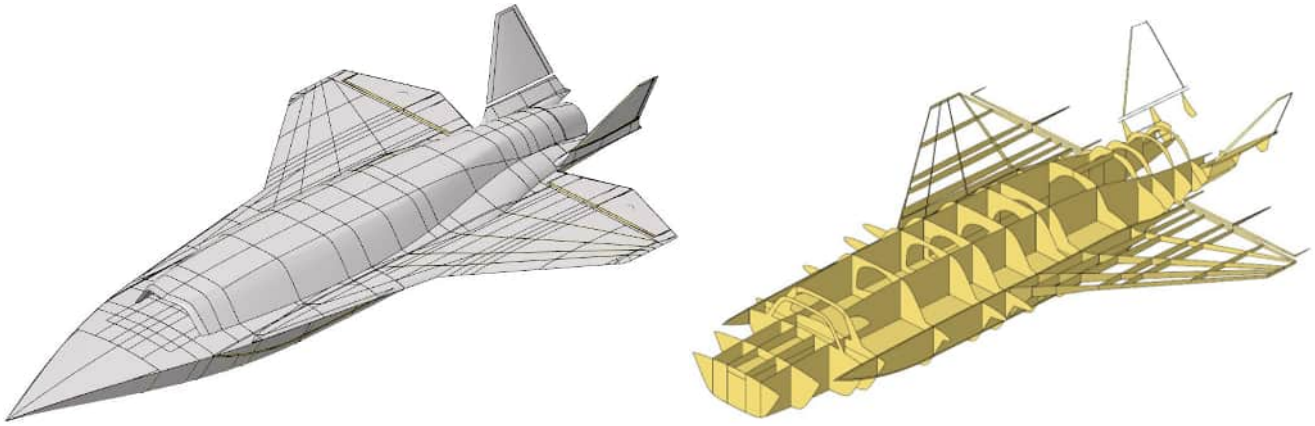

(a) Complete aircraft model. **(b)** Inside of the aircraft.

Figure 13: The unaltered generic aircraft structure.

Figure 13 illustrates the unaltered generic aircraft structure. The generic CAD model required clean up and modification to suit the analysis. This involved patching surfaces together and removing irrelevant features of the aircraft that would increase computational time. Since the region around the IWB is of greatest interest, the wings and fins were completely removed. Additionally, two frames were added to make the distance between the frames more realistic and the leading spar was moved to connect to the frame.

When everything was connected correctly, reinforcements were added to the surfaces. The distance between the reinforcements is 150 mm, based on the analysis of the downstream wall. This distance remains constant throughout the aircraft. The reinforcements are symmetrically placed on each surface based on the global coordinate system to ensure that they are connected to each other where structural components are connected. The reinforcements were created in the same way as for the downstream wall, by splitting the surface into multiple surfaces according to where the reinforcements should be positioned. Reinforcements were then implemented on the split line using 1D elements to increase the stiffness of the structural component. This was done to increase the stiffness and to get a more accurate dynamic behaviour of the aircraft structure. The IWB reinforcements are based on the result from the analysis of the downstream wall (part one) and have the same design regarding the height and thickness of the reinforcement, 2.5x25 mm. The reinforcements on the rest of the aircraft structure have height and thickness of 2.2x22 mm.

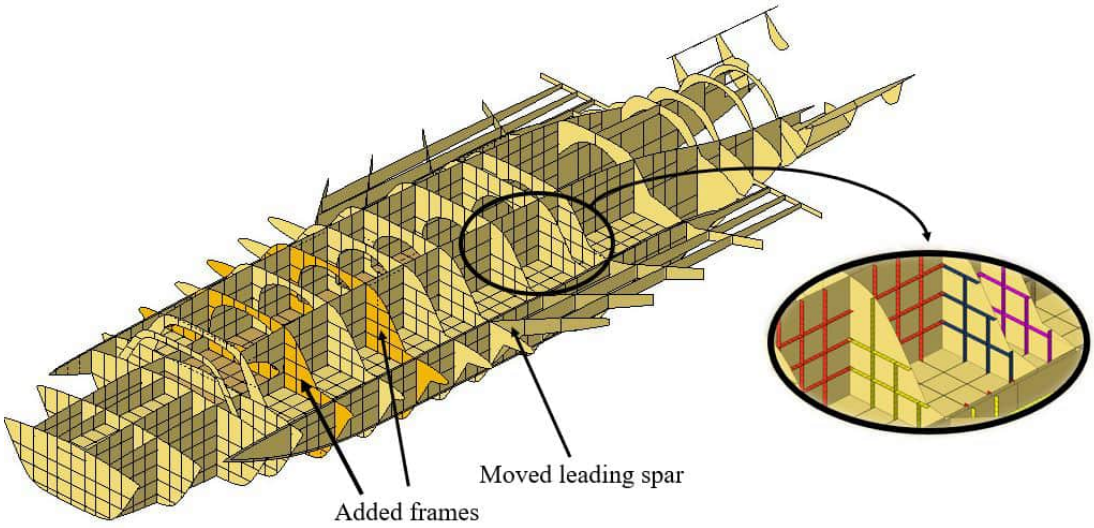

Figure 14: Updated geometry model. The updated frames and leading spar are visible. The circle shows how the reinforcement is attached to the surface.

Figure 14 shows the updated aircraft structure used for simulations. The three arrows point to the two frames added and the leading spar that has been moved. The split lines on the surfaces used to position the reinforcements can also be seen as well as a display of how the reinforcements are attached with the surface. The reinforcements are offset to one side of the surface, to avoid both tension and compression at the same time during load. On which side the reinforcements are offset is irrelevant except for on the IWB surface where consideration have to be taking regarding the position of the damping mats, which should be attached to the outside of the IWB. Therefore the reinforcements on the IWB are offset to the inside.

3.2.2 Structural components of the aircraft

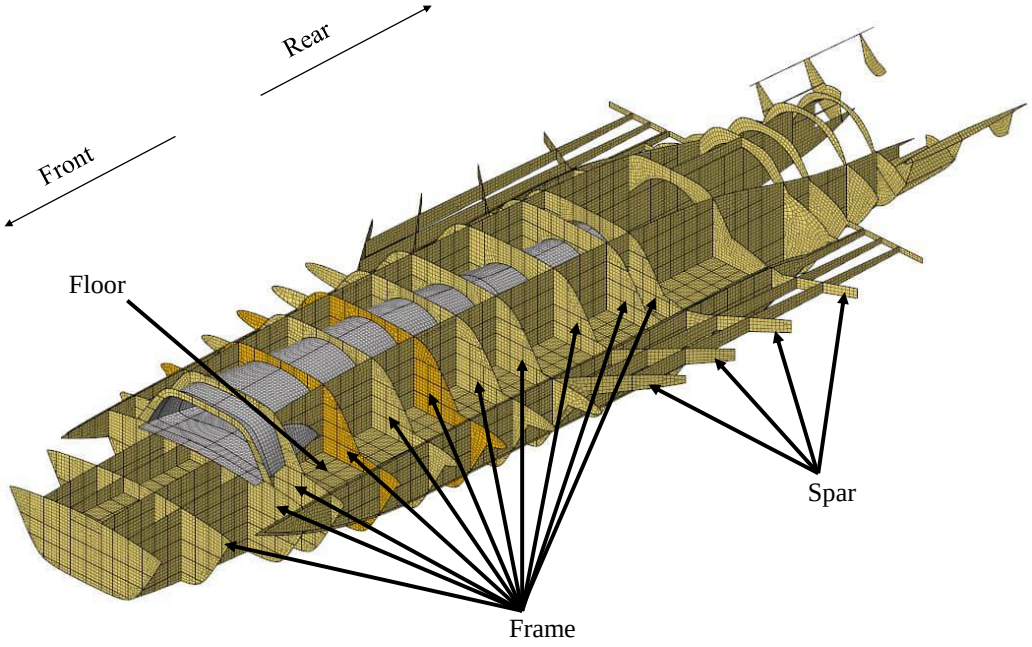

Figure 15: Aircraft seen from above with the fuselage hidden.

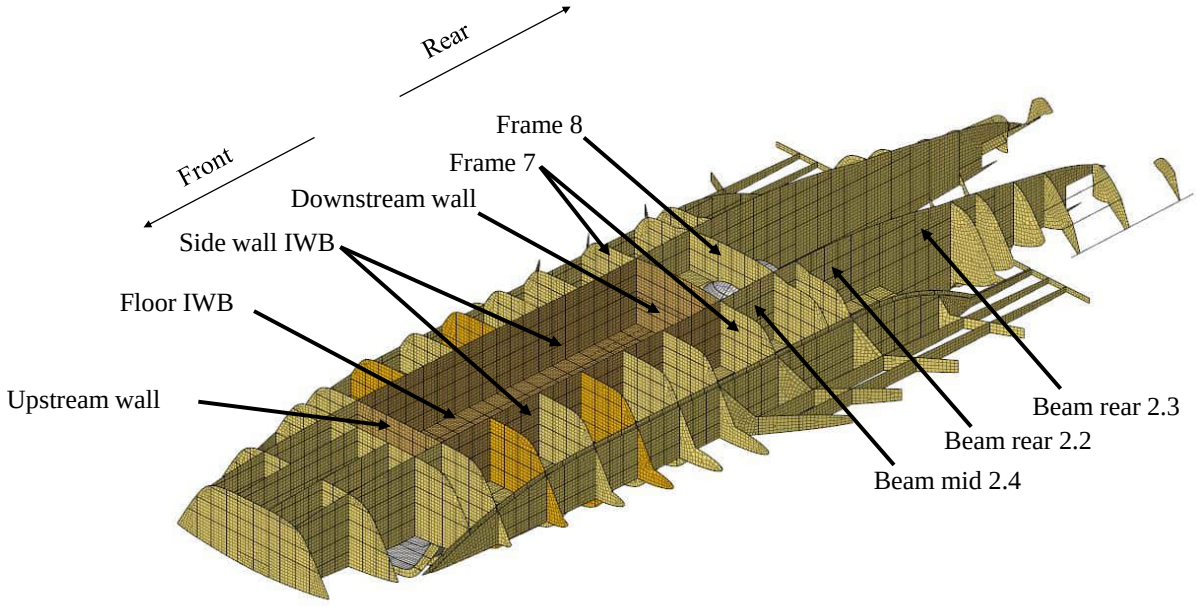

Figure 16: Aircraft seen from below with the fuselage hidden.

Figures 15 and 16 show the most important structural components used during this work. Figure 15 shows the aircraft from above and Figure 16 shows the aircraft from below with fuselage hidden.

3.2.3 Boundary conditions and mesh

To simulate an aircraft flying in the air, a free-free boundary condition is assumed meaning that no boundary conditions are applied on the aircraft. This leads to six rigid body modes for the modal analysis that are ignored.

The aircraft is meshed using first order shell elements and the mesh consists of mix between quadratic and triangular elements. The desired element size for the whole aircraft is 30 mm. This is seen as a good balance between computational time and accuracy.

3.2.4 Material data and structural thickness

All structural components of the aircraft are modelled as aluminium with the material data described in Table 2. The structural damping for the entire aircraft is set to 10%. This includes internal material damping, connections between structural components, and for example equipment that affects the dynamic environment, for instance cablings.

The thickness of the surfaces of the aircraft differs for different structural components. Table 3 shows the thicknesses for different sections of the aircraft.

Table 3: The thickness used for the different structural sections of the aircraft.

Structural components	**Thickness [mm]**
Fuselage	2.6
Longitudinal beams	4.0-15.0
Frames	4.0
Intake	2.6
IWB	2.5
Spar	2.0
Beak	2.6

3.2.5 Modal analysis

A modal analysis was conducted to validate the first natural frequency of the downstream wall model for comparison with the results from the isolated downstream wall, analysed in part one of the thesis.

3.2.6 Point masses

In order to increase the fidelity of the model, various equipment such as engines, radar components, and gearboxes are added. These equipments are modelled as dimensionless point masses,

which occupy no physical space within the aircraft. The mass points adds mass in all three global directions and are modelled without moment of inertia. The point masses are attached to the node closest to their actual position in the aircraft. Normally, such equipments would be mounted over a larger surface area. To simulate this, each point mass is distributed to the nine nearest nodes by rigid elements. Consequently, the total mass of any equipment, regardless of its actual weight, is distributed across these nodes. To manage the imbalance caused by the large mass of the engine on one side only, its mass is split into two mass points and placed symmetrically on each side of the aircraft. Additionally, the mass that would have been contributed by the now-removed wings is represented using similar point masses.

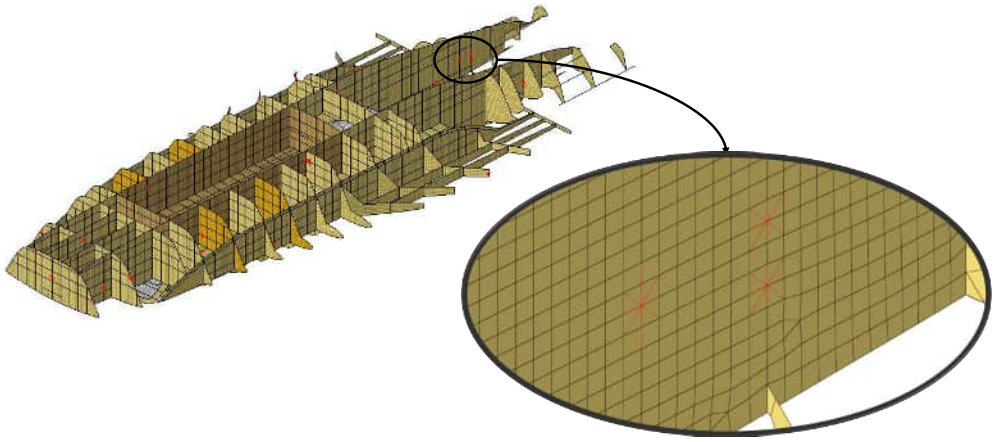

Figure 17: How point masses are implemented in the model. The point dimensionless mass is located in the centre of the point mass and the rigid elements are represented by red lines.

Figure 17 shows how point masses are implemented in the model. In the centre of the point mass, the dimensionless mass point is located. The mass is then connected to the surrounding nodes by the rigid elements, displayed by red lines.

This is modelled with CONM2 and RBE3 elements in Hypermesh. RBE3 (rigid elements) does not add stiffness to the model and thus only distribute the mass. How it is modelled in OptiStruct is described in more detail in the Appendix B.4 and B.5.

3.2.7 Excitation

The aircraft structure is excited by the cavity oscillations that arise from the aeroacoustic loads that emerge when the weapon bay doors are opened during flight. The excitation is calculated as in Chapter 3.1 from the standard ESDU 18011 in the range 10-2000 Hz. However, since the entire bay is used in this case, considerations must be given to the position along the bay since

the load will increase along the length of the IWB, from the upstream wall to the downstream wall. To capture this behaviour, the bay is divided into 12 zones along the cavity downstream direction, where the upstream and downstream wall are treated as separate zones. The excitation is dependent on the position along length of IWB where the sound pressure will rise from upstream wall to the downstream wall. To account for this behaviour the centre point in each zone (in the longitudinal direction) is used to calculate the excitation for each zone.

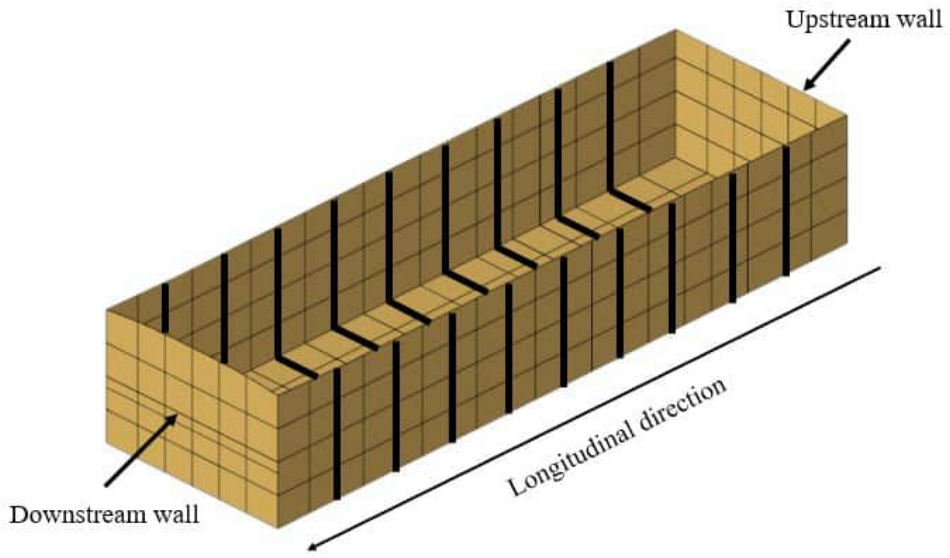

Figure 18: The 12 excitation zones. The zones are divided by the black lines along with the downstream and upstream walls.

Figure 18 shows the IWB and the 12 zones into which it is divided. The corresponding excitation is then calculated for each zone using the ESDU 18011 standard. The same flight parameters as for the downstream wall model is used, see Table 1.

3.2.8 Modelling fuel

In an aircraft, fuel is distributed throughout the entire aircraft, but for simplification, fuel is only modelled on the IWB side walls and connecting floor to see the effect from the fuel around the IWB.

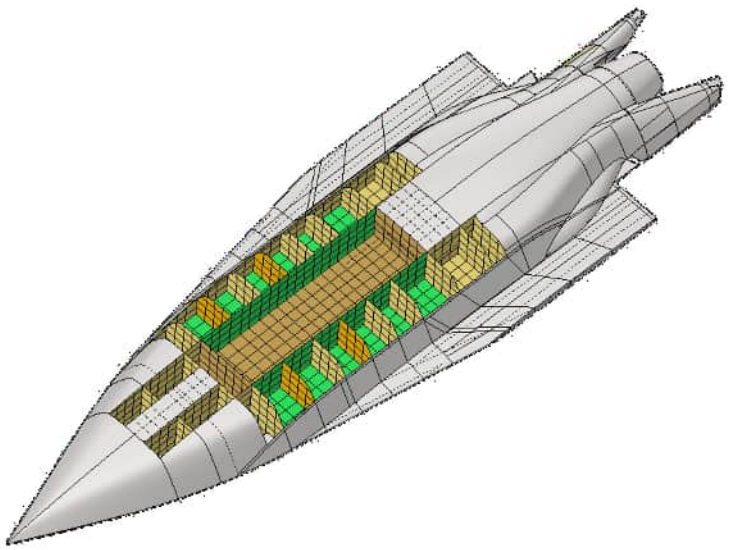

Figure 19: The green surfaces shows where the fuel is placed inside of the aircraft. The aircraft is seen upside down.

Figure 19 shows the surfaces where fuel is located. The density of the fuel is defined as 800 kg/m^3.

Fuel is modelled with the MFLUID load collector in OptiStruct. It is described in more detail in Appendix B.6.

3.2.9 Specification requirement

If equipment is to be mounted in the aircraft structure, it is important to know the maximum allowed vibrational amplitude for the component to avoid breakage. In this work, this is assumed to be 0.1 g^2/Hz in the frequency range 10-2000 Hz. This limit is used as a general guideline to gauge the validity of the results.

3.2.10 Vibrational response in the frequency range 10-2000 Hz

The vibration propagation and PSD response of the aircraft structure was calculated and compared against the specification requirement. Since high frequencies are to be analysed, the direct method was used to calculate the vibrational response.

The vibrational response figures are used to analyse the difference between the reinforcement and skin field in vibration propagation throughout the aircraft. Excitation based on the ESDU 18011 standard, point masses, and fuel are used in the baseline model.

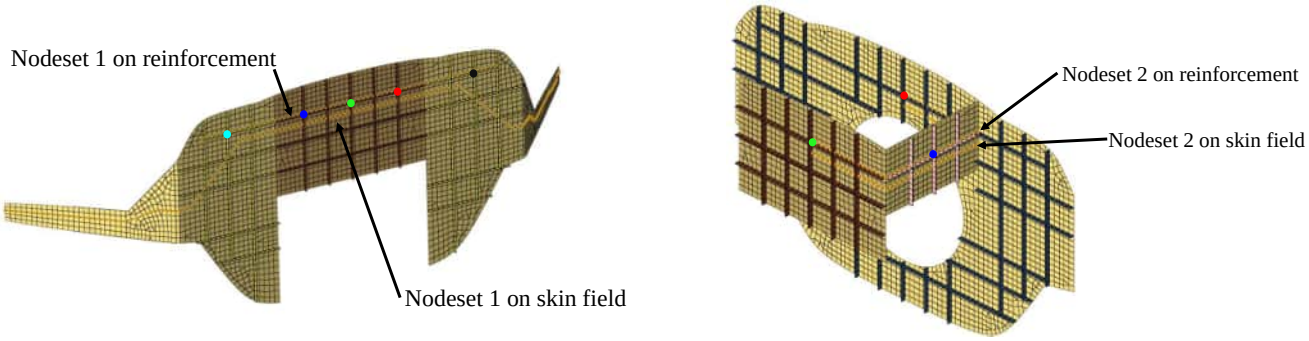

(a) Node set 1. **(b)** Node set 2.

Figure 20: Node sets 1 and 2 used to analyse the vibrational response. The coloured points indicates locations in which PSD over the whole frequency span was investigated.

Figure 20 shows node set 1 and 2 used to analyse the vibrational response of the aircraft. Node set 1 includes the downstream wall, Frame 7 and spar while node set 2 includes the downstream wall, Beam mid 2.4 and Frame 8. Note that the node set turns 90 degrees over some joints. For both node sets, the upper dotted line is located on the reinforcement while the lower dotted line lays on the skin field. Vibration propagation is plotted as PSD acceleration against length, where the length is normalised around the centre of the downstream wall. For both node sets 1 and 2, zero distance is thus the middle of the downstream wall.

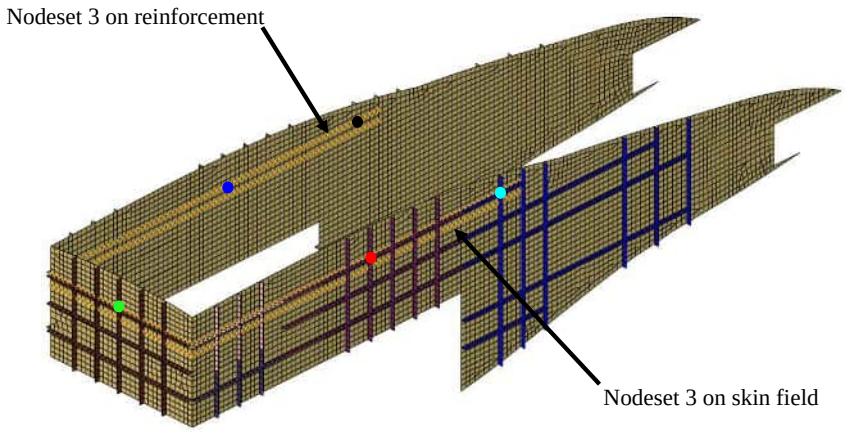

Figure 21: Node set 3 used to analyse the vibrational response. The coloured points indicates locations in which PSD over the whole frequency span was investigated.

Figure 21 shows node set 3 used to analyse the vibrational response. The structural components included in node set 3 are downstream wall, Beam mid 2.4, Beam rear 2.2 and Beam rear 2.3. Zero distance is the middle of the downstream wall.

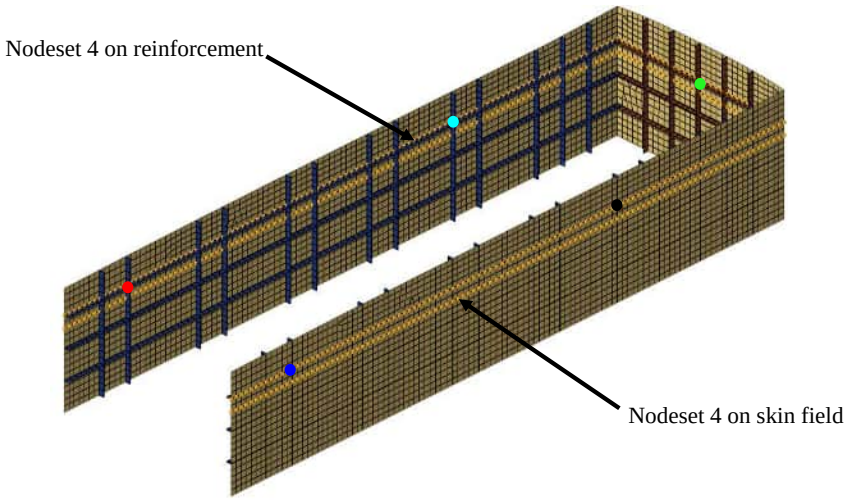

Figure 22: Node set 4 used to analyse the vibrational response. The coloured points indicates locations in which PSD over the whole frequency span was investigated.

Figure 22 shows node set 4 used to analyse the vibrational response of the aircraft structure. The structural components included in node set 3 are downstream wall and Side wall IWB. Zero distance is the middle of the downstream wall.

Simultaneously as the vibration propagation is analysed as a function of length the PSD over frequency is also investigated for points on reinforcement that belongs to their respective node set. node set 1,3 and 4 has five points along the node set while node set 2 has 3 points. The location of these points are seen in the figures. The result of each point has the same colour in the node set figures as in the plots.

3.2.11 Modelling damping mats

Damping mats are added to the back-half of the IWB since this is the part of the aircraft that is exposed to the highest vibration amplitudes based on ESDU 18011. The rubber is modelled as a frequency-dependent material where Young's modulus and the loss factor depend on the frequency.

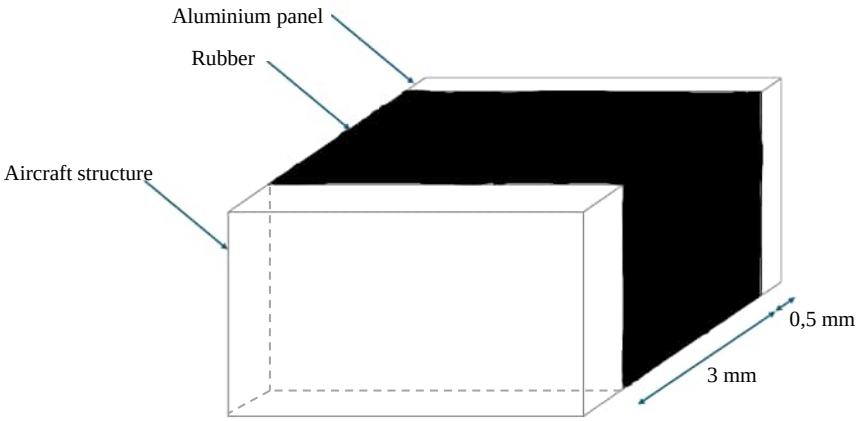

Figure 23: Illustration of the damping mat configuration.

Figure 23 shows the configuration of the damping pad. The pad material is modelled as nitrile rubber which is both frequency and temperature dependent.

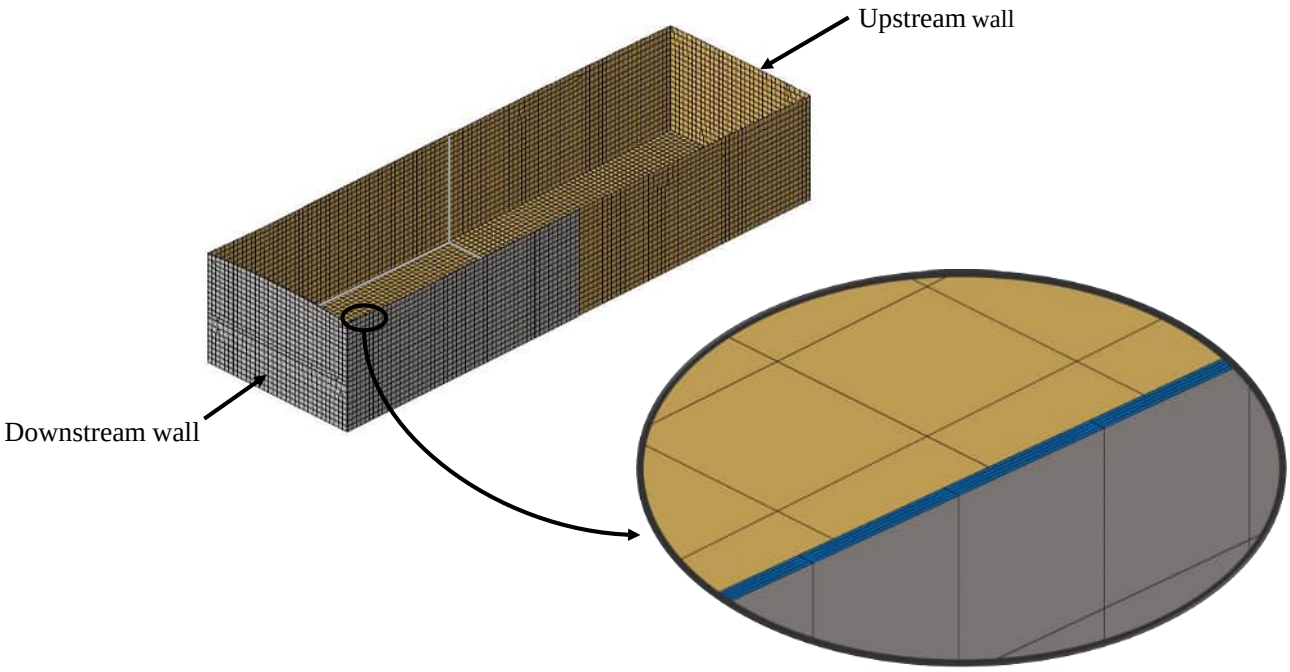

Figure 24: Illustrates the damping mats and how they are mounted at the IWB. The grey shell elements are the aluminium panel and the blue solid, hex8, elements are the rubber.

Figure 24 shows the damping mat and how they are mounted on the IWB.

The rubber damping mat is modelled with HEX8-elements. The mat is modelled with four elements in thickness to more accurately capture bending stress variations and thus the dissipation of energy. The aluminium panel is modelled in the same way as the rest of the aircraft, with shell elements.

Table 4: Material data for nitrile rubber [15]. The data is assumed constant between 1000-2000Hz.

Frequency [Hz]	Young's modulus [MPa]	Temperature [°C]	Density [kg/m^3]	ν [-]	Loss factor η [-]
10	27.6	10	920	0.499	0.25
100	41.37	10	920	0.499	0.5
1000	89.63	10	920	0.499	1
2000	89.63	10	920	0.499	1

Table 4 shows the material data for the rubber used in the damping mat. A constant temperature of 10 degrees Celsius is chosen for simplification. The Young's modulus and loss factor varies over the frequency span. [10]

For the aluminium panel, the same aluminium material data as the rest of the aircraft is used. The data of this material is described in Table 2.

The effect of damping mats is investigated through analysing the PSD over the frequency range for node sets 1-4. The colour of the curves corresponds to the nodes within each node set, using the same colour as the points in Figures 20-22 for clarity. The rubber material of the damping mat has a thickness of 3 mm, and the aluminium panel has a thickness of 0.5 mm. This analysis demonstrates how the damping mats influence the vibrational response, both locally and at more distant points.

To further investigate the damping mats, PSD and RMS acceleration plots are created to analyse how different parameters impacts the vibrational response. The parameters analysed are Young's modulus and the loss factor as well as the thickness of the rubber and the aluminium panel. The result is compared with the baseline model, which consists of reinforcements, point masses, and fuel. Two subplots are created for the three cases, where the first shows the response on the reinforcement and the second shows the affect on the skin field. The result is analysed for the baseline model and model with damping mats where Young's modulus and the loss factor in Table 4 are multiplied by 0.5, 1, 2 and 3. The thickness of the rubber was analysed as well for thicknesses of 1.5, 3 and 6 mm and the thickness of the aluminium panel is analysed for a thickness of 0.25, 0.5, 1 and 1.5 mm. The standard damping mat model has a rubber thickness of 3 mm and a aluminium panel thickness of 0.5 mm.

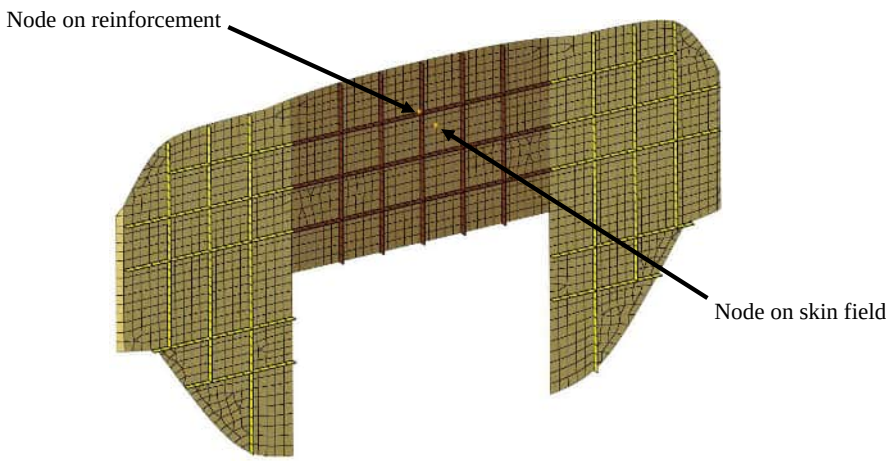

Figure 25: Two nodes on the downstream wall component that is used to analyse material parameters for the damping mats. One node is located on the reinforcement and one node is located on the skin field.

Figure 25 shows the two nodes on the downstream wall that are used to analyse the material parameters of the damping mats. They are located on the zone most exposed to high vibrational amplitude. The upper left node is located on the reinforcement and the lower right node is located on the skin field.

In the RMS figures, the horizontal axis is flipped. Consequently, the cumulative sum begins at 2000 Hz and concludes at 10 Hz. This arrangement is due to the fact that lower frequencies exhibit the highest amplitudes. As a result, visualizing the impact of higher frequencies becomes challenging.

3.3 Impact of equipment mounting position

To explore the effects of installing equipment on the vibrational behaviour of the aircraft, an analysis was conducted using a simplified version of the baseline model, in which point masses and virtual fluid mass were omitted. Two potential mounting points were identified on what is specified as Frame 8 in Figure 15.

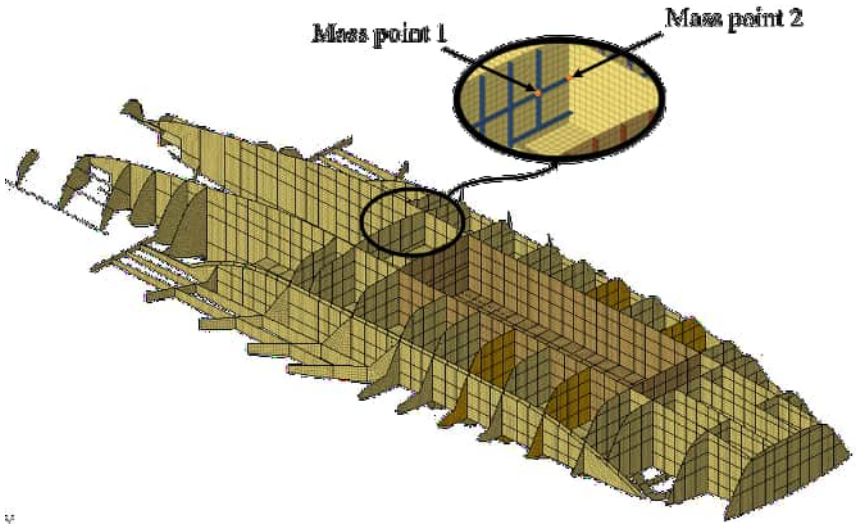

Figure 26: The placement of the mountings of equipments. The two different points are referred to as Mass point 1 and Mass point 2.

The position of the points can be seen in Figure 26. The points are chosen on the reinforcement to better represent realistic conditions. Mass point 2 is placed in the seam providing a stiffer configuration compared to Mass point 1. This enables comparisons between how the local stiffness's in the mounting points impacts the behaviour. The mass points are then excited with a unit load in three directions x,y and z and a unit pressure is applied to the whole IWB. The excitation's are constant between 10 and 2000 Hz.

This is done to obtain the Frequency response function of the structure for the combined case of force from mass and external pressure. With the FRF the PSD accelerational response throughout the aircraft can be calculated for different values of mass in the mass points using the theory outlined in Chapter 2.2.5. The mass was investigated for 0, 5, 10 and, 20 kg.

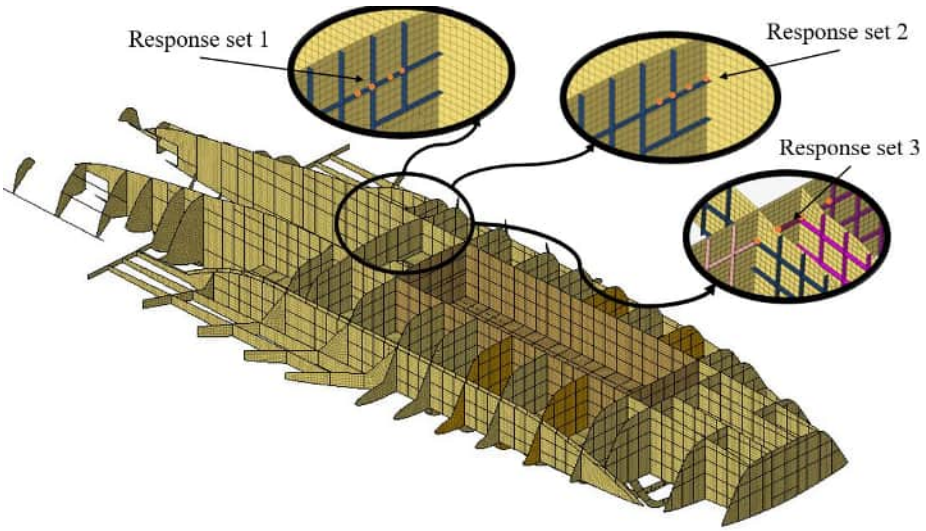

Figure 27: The three sets and their respective nodes where response was measured.

The response points chosen for the investigation of the impact of the mass is seen in Figure 27. The response points were placed relatively close to the points where mass was placed observe the behaviour locally.

3.4 Validation

The model validation involves analysing the PSD response and excitation of the downstream wall in comparison with NASA Handbook 7005, which includes an extrapolation curve derived from experimental data across various aerospace vehicles. The empirical solution is an extrapolated curve based on investigations made by NASA that shows how much the structure vibrates (in dB) based on its surface density.

Comparison of the PSD excitation curve (expressed in dB) with the PSD response of the downstream wall (measured in g^2/Hz) requires the definition of surface density.

4 Results and Discussion

4.1 PSD excitation

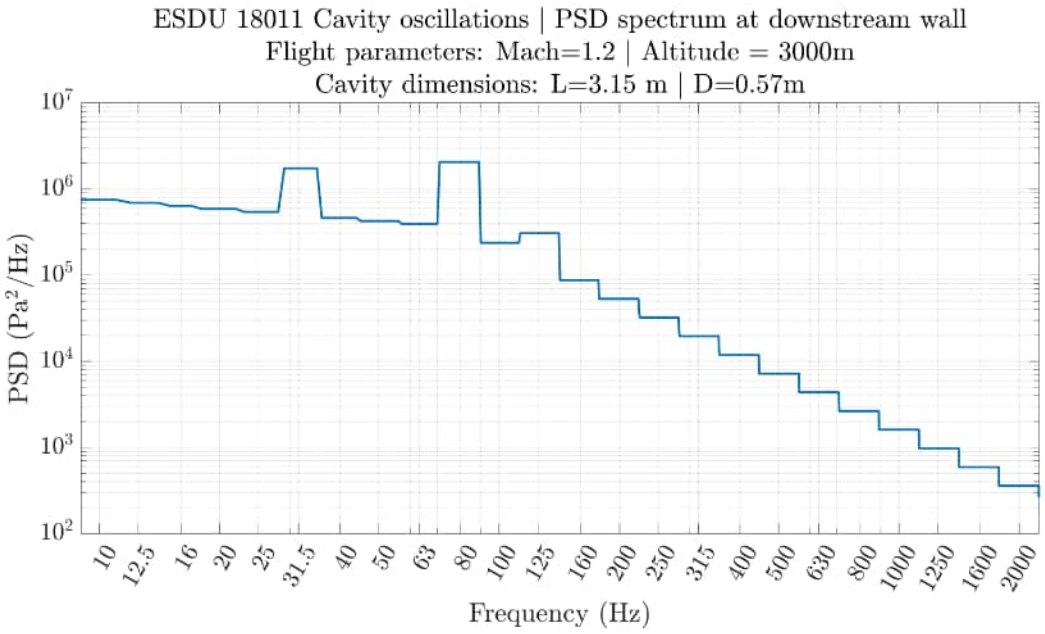

Figure 28: PSD excitation for the downstream wall according to ESDU 18011 with flight parameters and cavity dimensions. The spectrum is given in one-third-octave bands. The three Rossiter modes are visible at approximately 25, 80 and 125 Hz.

Figure 28 shows the PSD excitation for the downstream wall in one-third-octave bands. This is used as input load on the downstream wall model. For part two of the work the PSD excitation is scaled according to its longitudinal position in the cavity (x/L ratio). Note that the three Rossiter modes (approximately: 25, 80 and 125 Hz) are the most energetic and that the PSD excitation decreases for higher frequencies.

4.2 Designing the downstream wall

The first step is analysing the first natural frequency for the downstream wall with a reinforcement dimension of 2.2x22 mm.

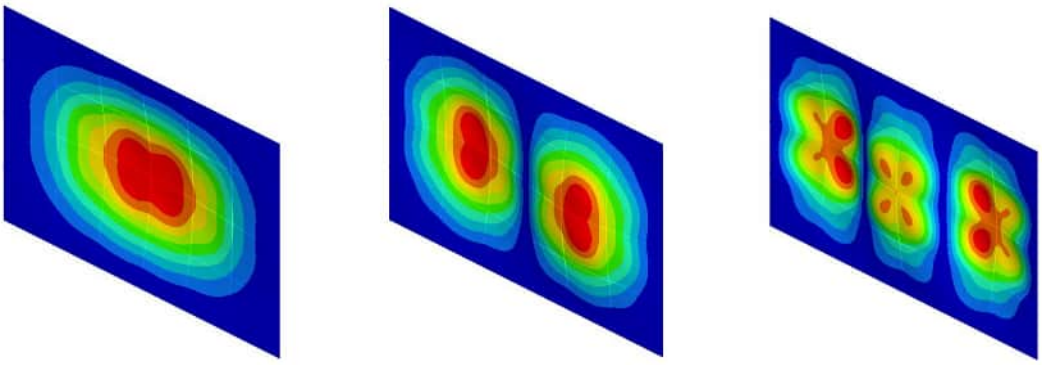

Figure 29: First three modes and its corresponding natural frequency for a reinforcement dimension of 2.2x22 mm.

Figure 29 illustrates the first three mode shapes along with their respective natural frequencies. The lowest natural frequency for the downstream wall is 223 Hz, while the third Rossiter mode occurs at 122.6 Hz. According to Equation (19), 223 Hz $\geq$ 183.9 Hz, resonance is thus avoided. The results indicate that adding reinforcements causes significant localization on the skin-field starting as early as mode 3.

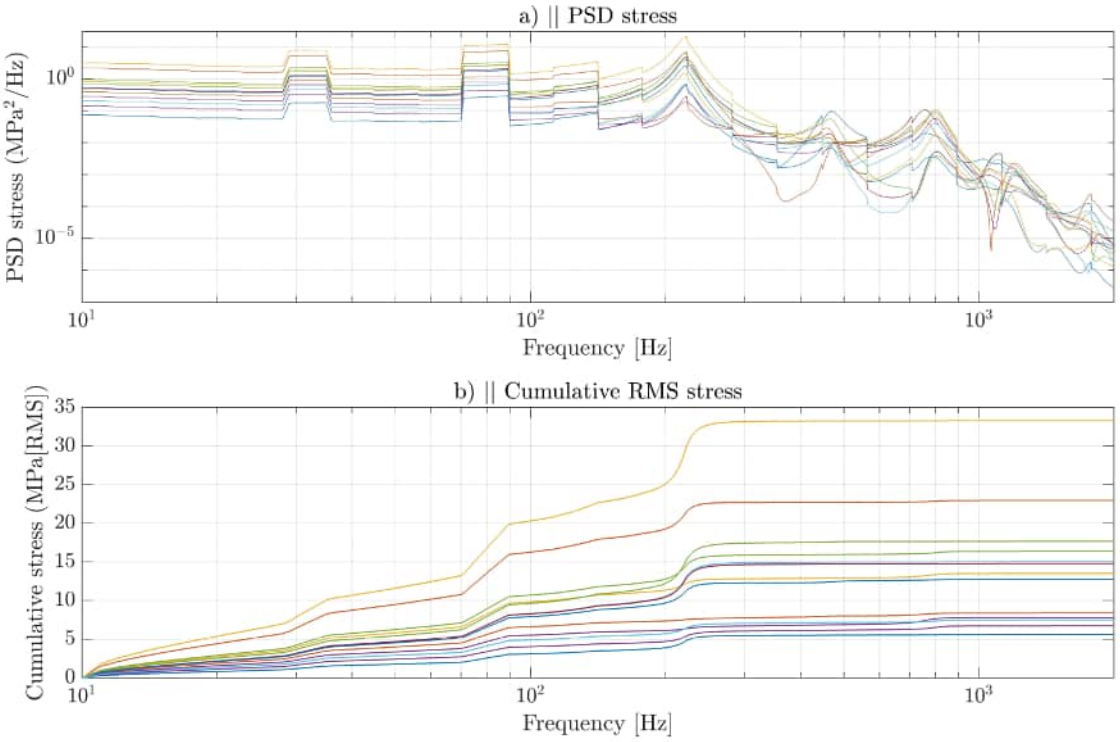

Figure 30: PSD stress and cumulative RMS stress for a reinforcement dimension of 2.2x22 mm. Subplot a) shows the PSD stress over the frequency range and subplot b) shows the cumulative RMS stress over the frequency range for the downstream wall. Each line represents one element in Figure 12.

Figure 30 illustrates the variations in PSD stress and cumulative RMS stress across the frequency range for the elements depicted in Figure 12. Subplot a) shows that the three Rossiter modes occur at frequencies lower than the first natural frequency. Subplot b) presents the cumulative RMS stress for the downstream wall, indicating that the stress accumulates with frequency. The maximum RMS stress for the downstream wall reaches 33 MPa, thereby exceeding the three-sigma design criterion.

The reinforcements implemented on the downstream wall is then updated and analysed for a dimension of 2.5x25 mm.

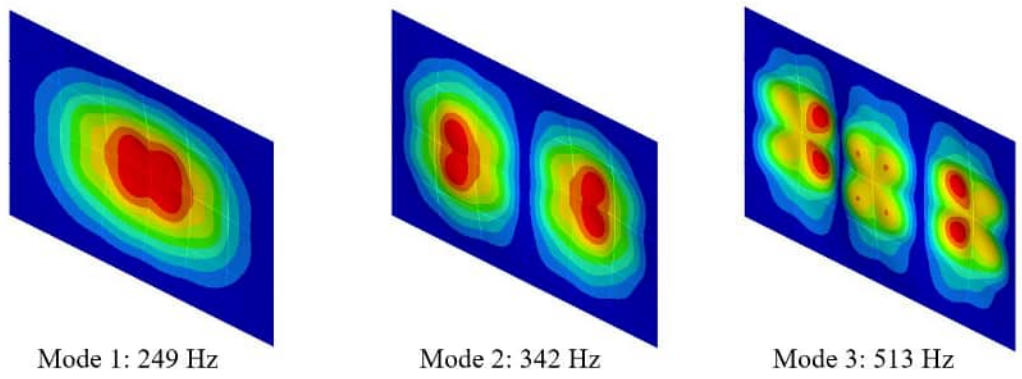

Figure 31: First three modes and its corresponding natural frequency for a reinforcement dimension of 2.5x25 mm.

Figure 31 shows the first three modes and its corresponding natural frequency. The first natural frequency is 249 Hz and the third Rossiter mode is 122.6 Hz. Equation (19) gives that, 249 Hz $\geq$ 183.9 Hz, thus implying that resonance is avoided.

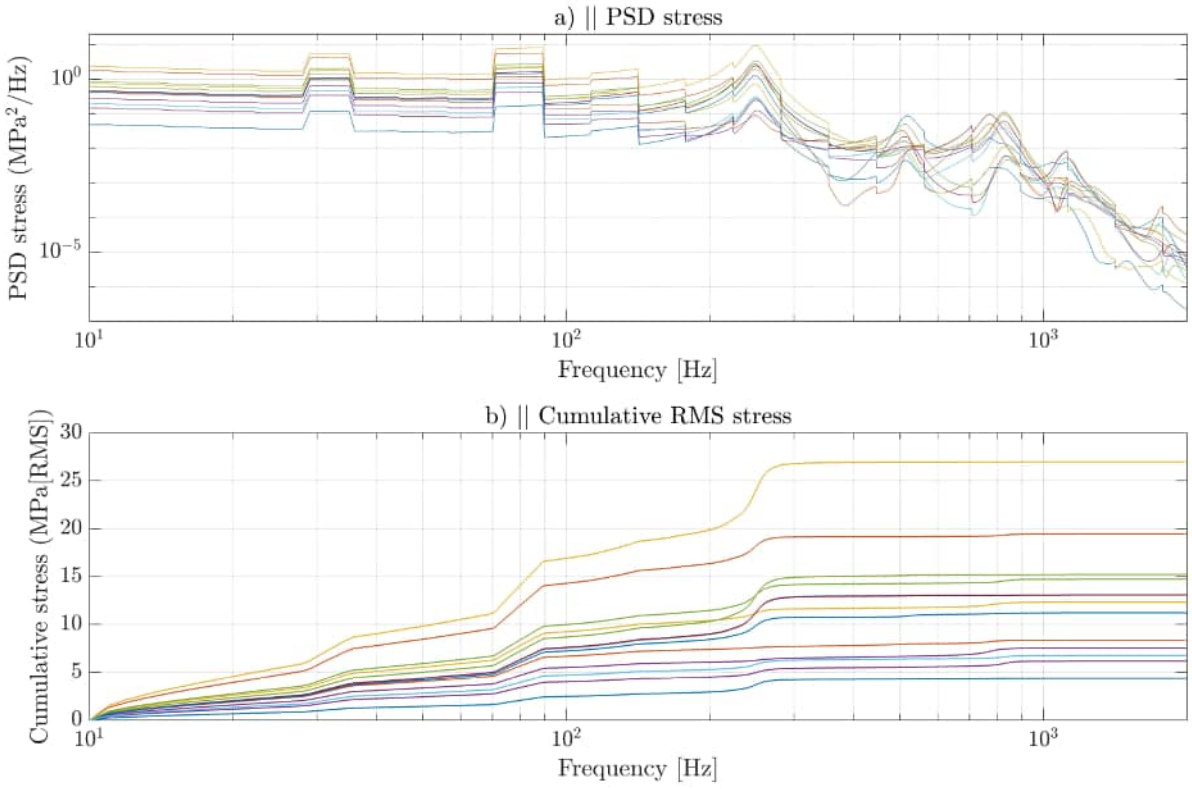

Figure 32: PSD stress and cumulative RMS stress for a reinforcement dimension of 2.5x25 mm. Subplot a) shows the PSD stress over the frequency range and subplot b) shows the cumulative RMS stress over the frequency range for the downstream wall. Each line represents one element in Figure 12.

Figure 32 presents the PSD and cumulative RMS stress for the downstream wall. Subplot a) indicates that the third Rossiter mode occurs at a lower frequency than the first natural frequency. Subplot b) shows that the maximum cumulative RMS stress is 27 MPa. As a result, the three-sigma design criterion is met, and thus avoiding fatigue. Consequently, the reinforcement dimensions are adopted for the IWB in the global model.

From the two RMS plots in Figures 30 and 32 it is observed that the RMS stress increases significantly at the Rossiter modes and up until the first natural frequency of the downstream wall. Beyond the first natural frequency, the stress does not increase significantly, suggesting that the higher modes are less energetic. This suggest that when analysing the downstream wall, the concentration of stress is found for lower frequencies.

Designing the downstream wall involved an iterative process with multiple adjustable input parameters to meet resonance and fatigue conditions. Two of these parameters were the thickness of the downstream wall and the reinforcement pattern. To simplify the design process, the thickness and pattern were determined based on practical considerations, and their impact was not analysed further. There is a relationship between these parameters and the reinforcement dimensions; altering the thickness of the downstream wall or the reinforcement pattern would allow changes in the reinforcement dimensions.

The three-sigma design criterion was the critical condition compared to avoiding resonance. This means that the reinforcement design was based on the RMS results. The most conservative result from aluminium in ESDU FAT E.07.01 was used to determine the fatigue limit.

1D beam elements were chosen to model the reinforcements. Although 2D shell elements were considered, the simplicity of modelling 1D elements made them the superior choice for the reinforcements, particularly given the extensive implementation of reinforcements within the aircraft structure.

4.3 Vibration environment of aircraft structure

4.3.1 Modal analysis

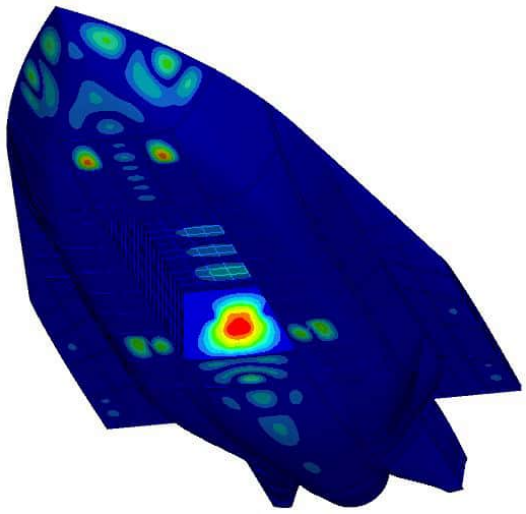

Figure 33: The response of the whole aircraft at 228 Hz. The eigenmode associated with the downstream wall is clearly visible.

The deformation of the downstream wall in Figure 33 resembles the first eigenmode of the downstream wall model. The natural frequency of the aircraft structure at that particular eigenmode is 228 Hz. The first eigenfrequency for the downstream wall model in part 1 for the same reinforcement dimension was 249 Hz leading to a difference of 21 Hz.

The downstream wall of the aircraft features two shelves mounted between Frame 7 and Frame 8. These shelves noticeably affect the downstream wall in the modal analysis of the entire aircraft. This is evidenced by a symmetrical tapering of relative displacement at the connection between the shelves and downstream wall. While these shelves were not accounted for in the downstream wall analysis conducted in the initial phase, their impact on the results suggests their inclusion would be advantageous for future analyses of a similar nature.

The difference in eigenmode frequency associated with the downstream wall between the aircraft model and the downstream wall model may be attributed to the implementation of stiffer boundary conditions in the downstream wall model. Specifically, the aircraft connection is modelled using a shared edge constraint, which appears to be less stiff compared to the fixed boundary condition.

4.3.2 Vibrational response in the frequency range 10-2000 Hz

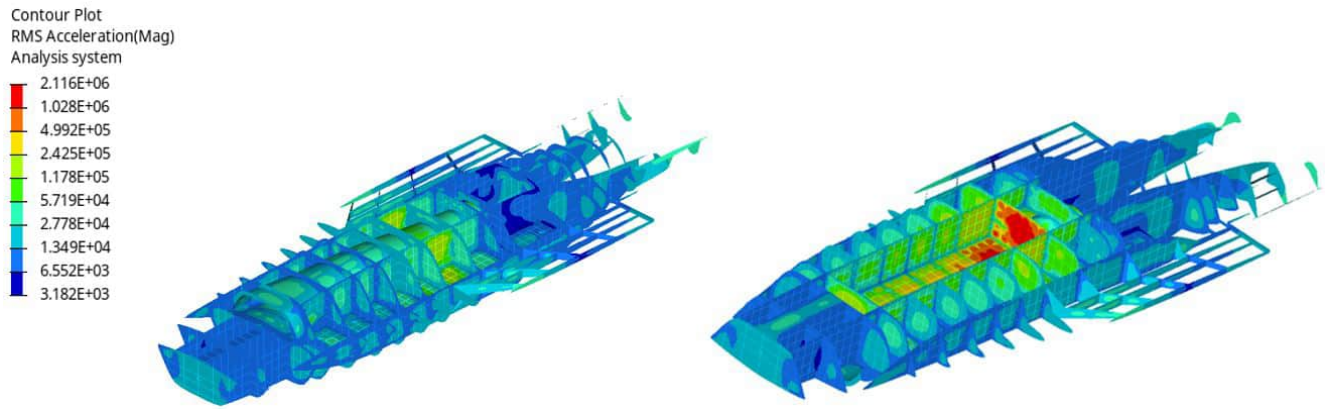

Figure 34: RMS contour plots showing the RMS acceleration in logarithmic scale for a frequency range of 10-2000 Hz. The values of the contour is given in (mm/s^2[RMS]).

Figure 34 displays the RMS acceleration contour plots in logarithmic scale for the inside of the aircraft structure. It is evident from the figure that the highest concentration of PSD acceleration between 10-2000 Hz is located in and around the vicinity of the downstream wall. It is visible that the vibrations that arise due to cavity oscillations will spread throughout the aircraft, and that the majority of the aircraft would have to be included in the analysis.

Subsequently, the vibrational response was analysed for the four node sets described in Figures 20-22, utilising the baseline model.

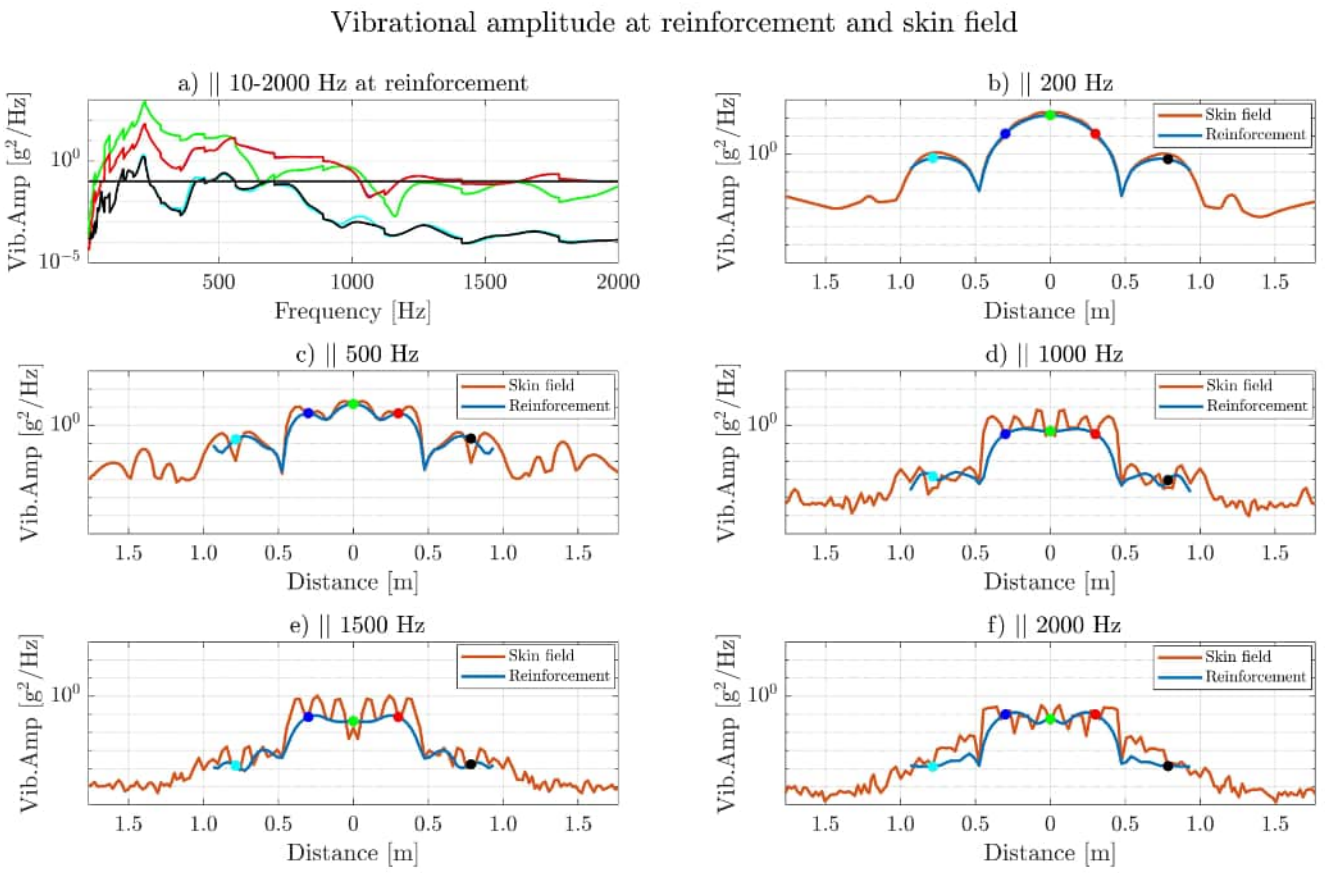

Figure 35: The subplot of vibration for node set 1. The colour of the lines in subplot a) corresponds to a node (point) displayed with the same colour in subplots b)-f). The centre of the downstream wall is located at distance zero. The horizontal black line indicates the specification requirement.

Figure 35 shows a subplot of the vibrational response for node set 1. Subplot a) illustrates how the vibrational amplitude of five nodes changes over the frequency span. The positions and colours of these nodes are displayed in subplots b)-f). Subplots b)-f) show the vibration propagation at one frequency. The highest amplitude for the five analysed frequencies occurs at 200 Hz. This is expected since the natural frequency of the downstream wall is 228 Hz, as shown in Figure 33 and that the excitation is higher for lower frequencies.

In subplot b), it can be seen that the reinforcement and the skin field vibrate together. In subplots d), e), and f), the skin field is more oscillative with an increase in amplitude compared to the reinforcement. This result is expected due to the local change in stiffness from the implementation of reinforcements.

The results in subplots b)-f) show that the vibration propagation decreases as it moves away from the middle of the downstream wall for all frequencies, and that the vibrations entering the wing are small compared to the vibrations on the downstream wall.

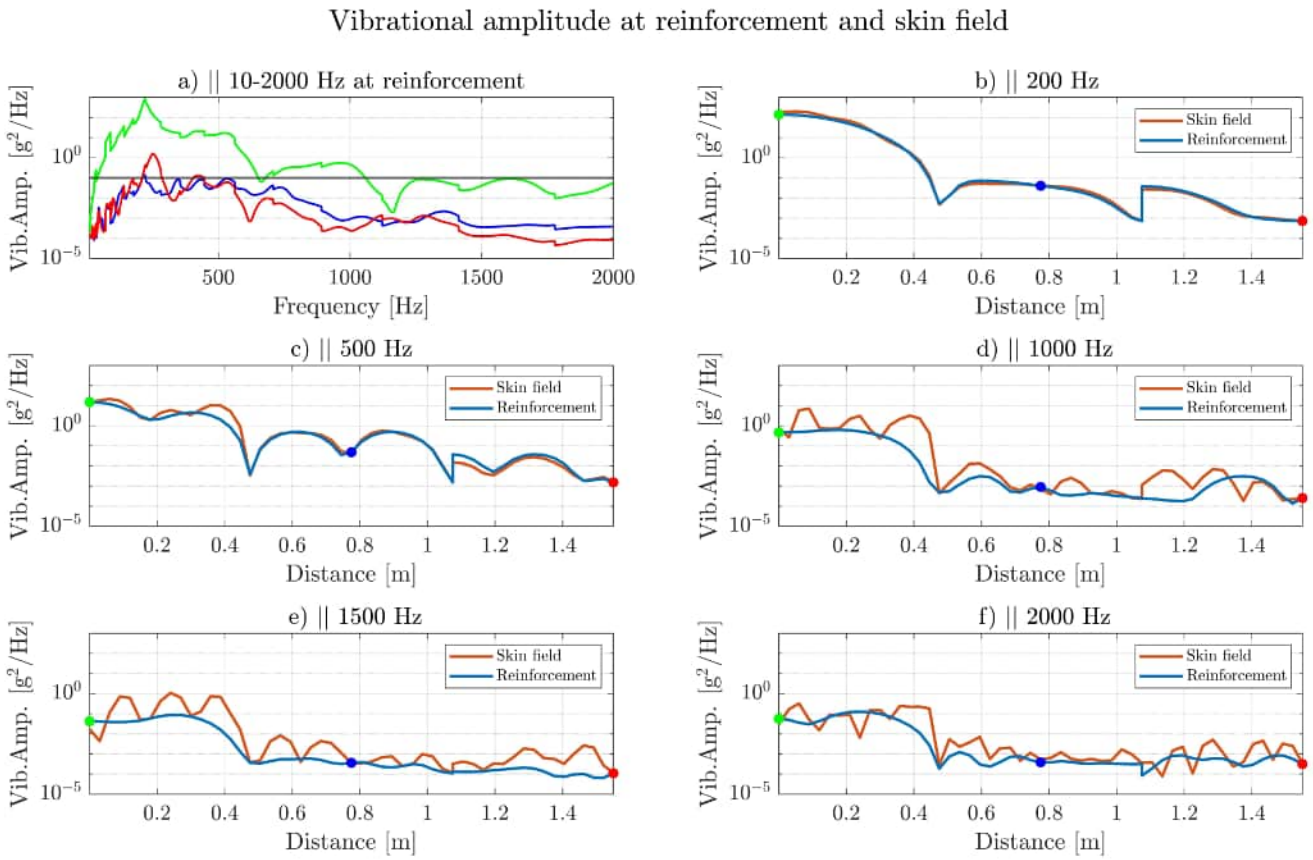

Figure 36: The subplot of vibration for node set 2. The colour of the lines in subplot a) corresponds to a node (point) displayed with the same colour in subplots b)-f). The centre of the downstream wall is located at distance zero. The horizontal black line indicates the specification requirement.

Figure 36 shows a subplot of the vibrational response for node set 2. Subplot a) illustrates how the vibrational amplitude of five nodes changes over the frequency span. The positions and colours of these nodes are displayed in subplots b)-f). Subplots b)-f) show the vibration propagation at one frequency. The highest amplitude for the five analysed frequencies occurs at 200 Hz. The difference in vibration propagation for higher frequencies, as seen in subplots d), e), and f), is small, with significant skin field resonance.

The result in subplots b)-f) does not decay as much for higher frequencies as the result subplots b)-f) in Figure 35.

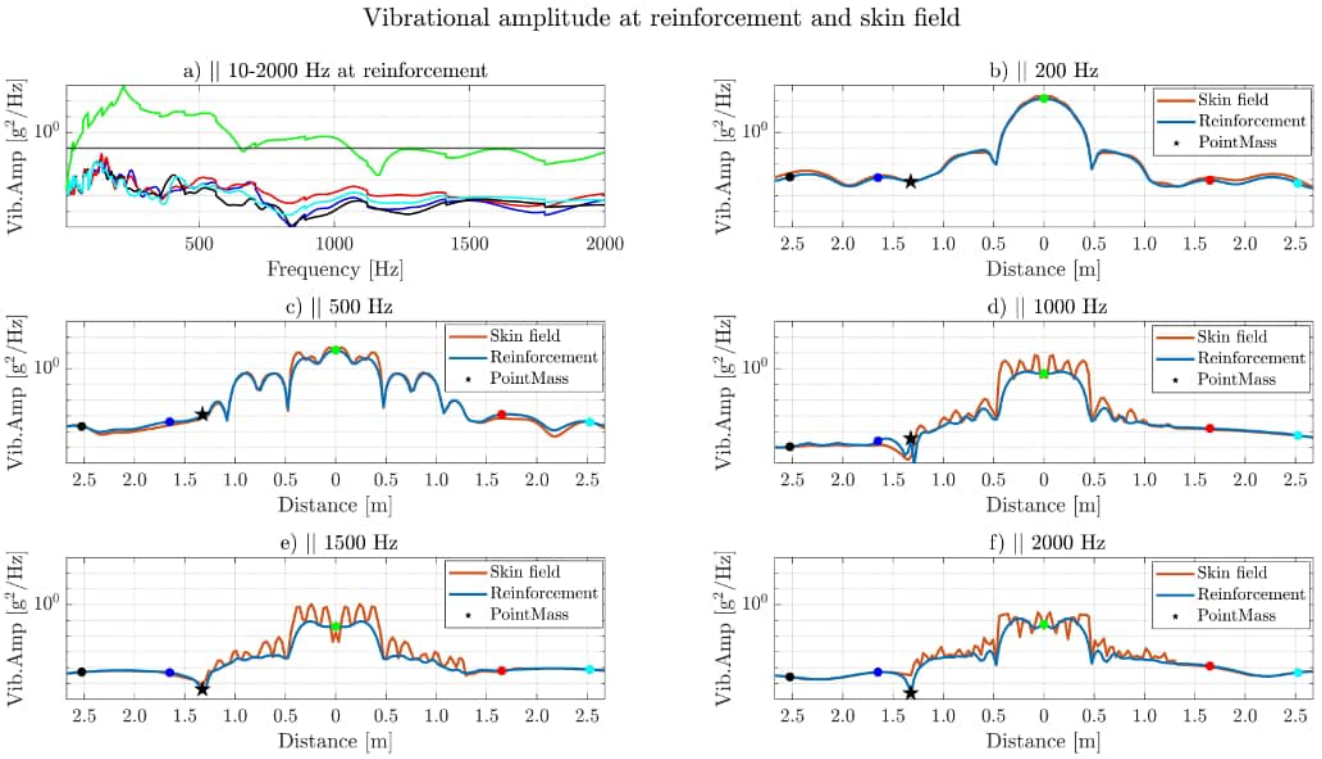

Figure 37: The subplot of vibration for node set 3. The colour of the lines in subplot a) corresponds to a node (point) displayed with the same colour in subplots b)-f). The centre of the downstream wall is located at distance zero. The horizontal black line indicates the specification requirement.

Figure 37 shows the vibrational response for node set 3. Subplot a) illustrates that for equipment placed outside the vicinity of the downstream wall, the requirement is met for the chosen node set. In node set 3, there is a point mass located 1.4 metres from the source, represented by a star in subplots b)-f). This point mass represents an equipment weighing 32 kg. The point mass significantly dampens the vibration propagation locally, especially for higher frequencies, but also has a lesser effect further out.

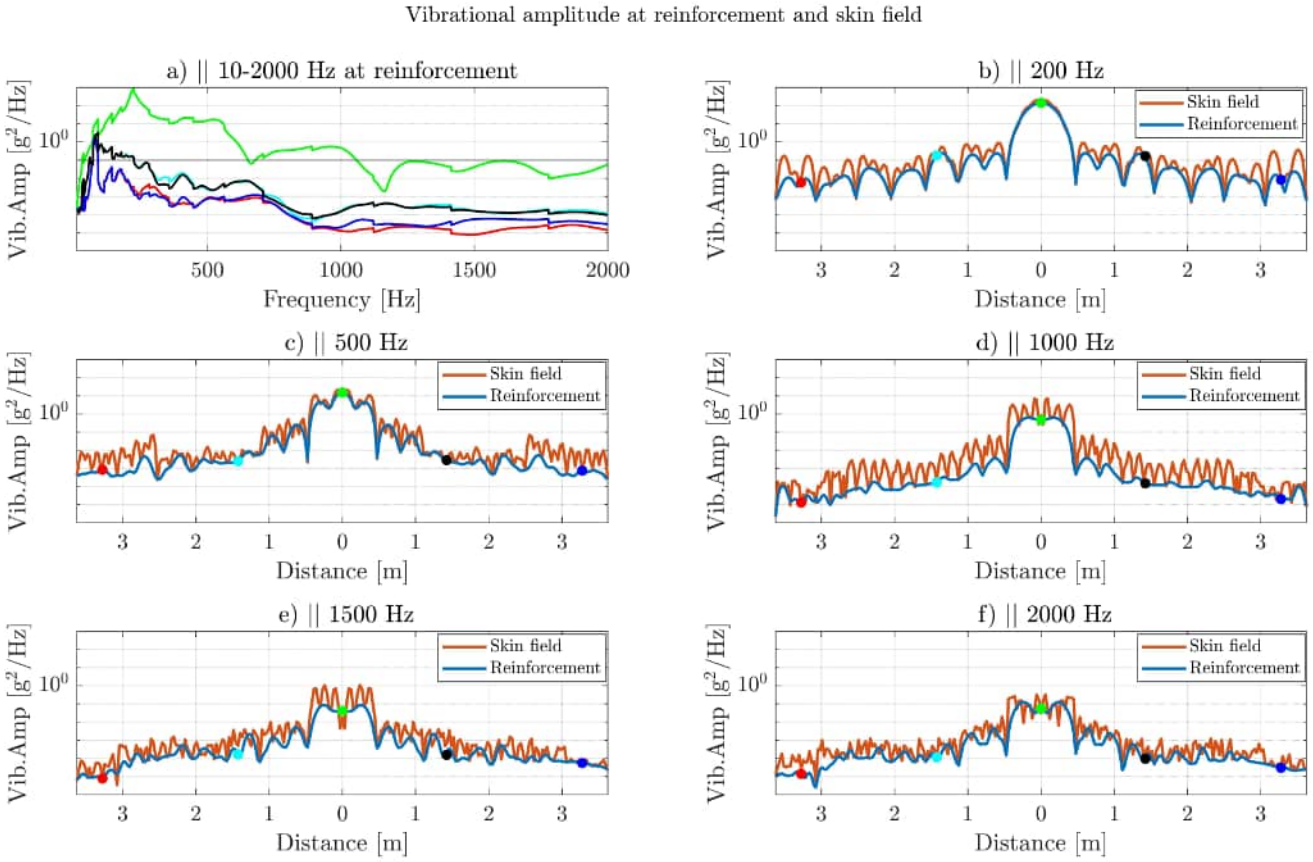

Figure 38: The subplot of vibration for node set 4. The colour of the lines in subplot a) corresponds to a node (point) displayed with the same colour in subplots b)-f). The centre of the downstream wall is located at distance zero. The horizontal black line indicates the specification requirement.

Figure 38 shows the vibrational response for node set 4. High amounts of localization in the skin field is seen in subplots b)-f), even for lower frequencies. This is probably due to the fact that the node set is located on excited surfaces. The sidewalls are also affected by the virtual fluid mass which represents fuel. The blue and black line in subplot a) (blue and black point in subplots b)-f)) exceeds the specification requirement indicating that equipment can not be mounted on the side wall in the vicinity of the downstream wall.

For Figure 38 the difference in excitation magnitude for the IWB between the downstream wall and the side walls in its closest vicinity is small. The dimensions of the walls are the same, as well as the reinforcements. This leads to the belief that the virtual fluid mass decreases the vibrational amplitude in the areas where it is applied.

For higher frequencies, the vibration propagation plots in Figures 35-38 show a lack of resolution, especially concerning the skin field. This is most likely caused by the element size being too large to capture wave propagation for small wavelengths. This issue could potentially be addressed by implementing smaller elements or elements of higher order, but this would significantly increase

computational time. However, since the bulk of the vibration response occurs in the lower half of the frequency span, the lower resolution for higher frequencies is accepted to reduce computational time.

In the analysis of the downstream wall from the first part, a similar result is observed but with a much denser mesh. Figures 30 and 32, where the analysis is conducted with an element size six times smaller, show that the cumulative RMS levels out for the upper half of the frequency span. The excitation applied to the IWB and downstream wall also decreases significantly over the frequency span. This makes it reasonable to believe that the most important effects are still captured with a smaller frequency span. However, if truly accurate results are required for the upper half of the frequency span, a denser mesh is necessary to capture the propagation accurately.

Regarding the specification requirement it can be noted that even though the downstream wall was designed conservatively the PSD acceleration in subplot a) in Figures 35-38 still does not pass the specification requirement. Indicating that equipment can not be mounted even on the reinforcement of the downstream wall without adding damping or increasing the stiffness of the downstream wall. For areas outside of the direct vicinity of the IWB the vibrational amplitude generally only exceeds the requirement at lower frequencies.

The details of the aircraft also impact the propagation, as is most clearly visible in subplot b) of Figure 38 and subplot c) of Figure 37, where the crossing of connecting frames leads to a rapid descent of the vibrational amplitude. This suggests that close to the IWB and especially the downstream wall, accurate modelling of the structure is needed. Further away from the IWB, the vibrational amplitude is low enough that the vibrational environment is insignificant compared to the specification requirements. When using only the ESDU 18011 standard as excitation in the analysis, it is therefore reasonable to remove the wings, the rear structure of the aircraft, and the structure in front of the IWB, based on Figure 35, with the latter two observable as having low RMS acceleration in Figure 34.

Figures 35-38 clearly show a significant difference between the skin field and reinforcement, particularly at higher frequencies. The reinforcement's contribution to stiffness is crucial for achieving the proper vibrational behaviour of the aircraft structure. Analysing a surface with actual reinforcements requires accurate modelling of these reinforcements to precisely capture vibrations and stress. The knowledge of designing and positioning reinforcements is comprehensive, and even minor dimensional variations can impact the vibrational environment, as noted in the RMS plots in Figures 30 and 32.

4.3.3 Modelling damping mats

Damping mats were installed on the downstream wall and on half of the side walls and floor of the IWB, as seen in Figure 24.

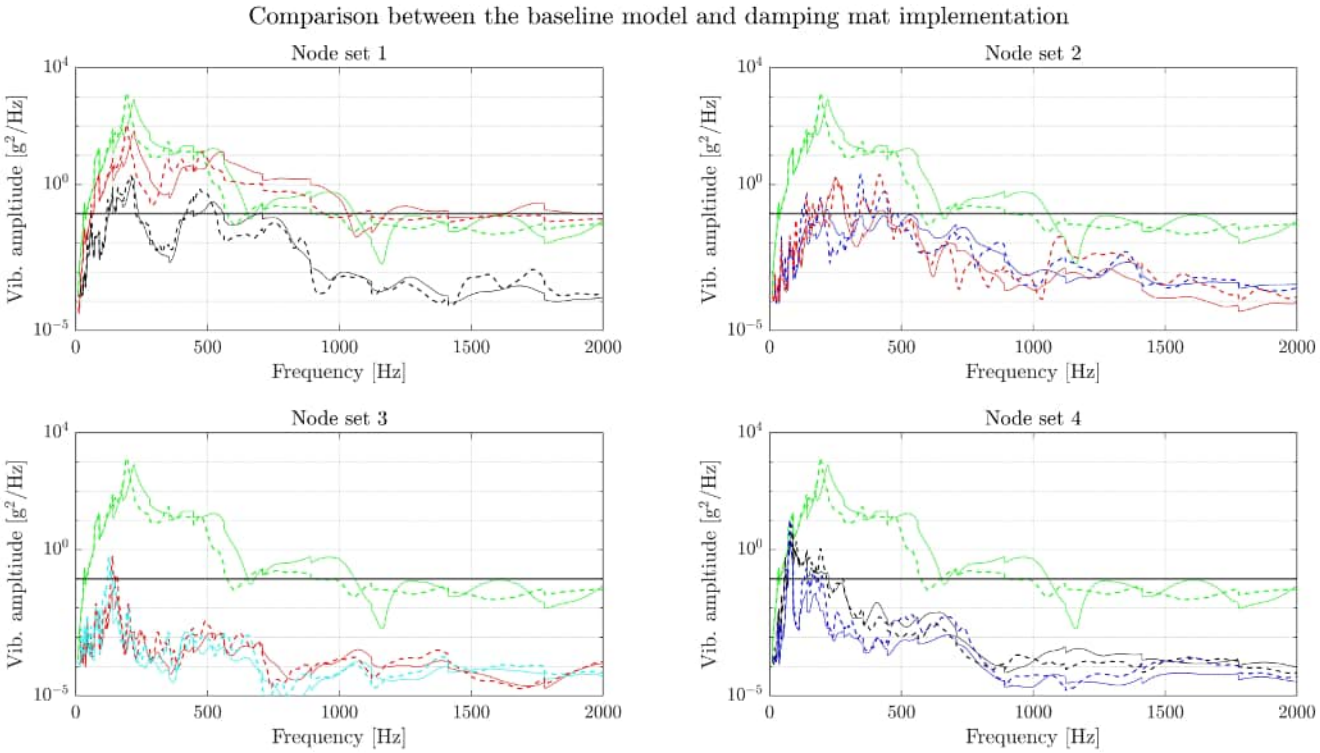

Figure 39: Comparison between the baseline model and damping mat model. The lines with the same colour represents the same point for the two compared configurations. The dotted line indicates that damping mats are applied and the solid lines is the baseline model. The colours of the lines represents a node in their respective node set with the same colour in Figures 20-22.

Figure 39 shows four subplots for node set 1-4 where the PSD acceleration over the frequency span is analysed for the baseline model and a configuration with damping mats. For all analysed nodes it is noted that the highest vibrational amplitude is found on the middle of the downstream wall.

From the results in node set 4, it is evident that the vibrational amplitude below 300 Hz exceeds the specification requirement, indicating that damping is necessary not only on the downstream wall but also on the side walls. Similarly, for the other cases, the vibrational amplitude exceeds the specification requirement below 400 Hz, suggesting that damping is required in those areas as well if equipment is to be mounted in this region of the aircraft.

From Figure 39, it is clear that installing damping mats affects the dynamic behaviour of the structure. This is observed for nodes both on the damping mats and at a distance. However, from this analysis, it remains unclear if this modelling approach for damping mats and their parameters effectively reduces the vibrational response of the aircraft. It should be noted that the nodes are located on the reinforcement, which is stiffer and thus less prone to shear compared to the skin field. To gain a deeper understanding of the damping mats and their impact on the vibrational environment, different parameters are tested and analysed.

To analyse the effect of damping mats and how their parameters affect energy dissipation, PSD acceleration and cumulative RMS acceleration were examined for the downstream wall, which experienced the highest vibrational amplitude. Two nodes, one on the reinforcement and one on the skin field, were analysed, as shown in Figure 25.

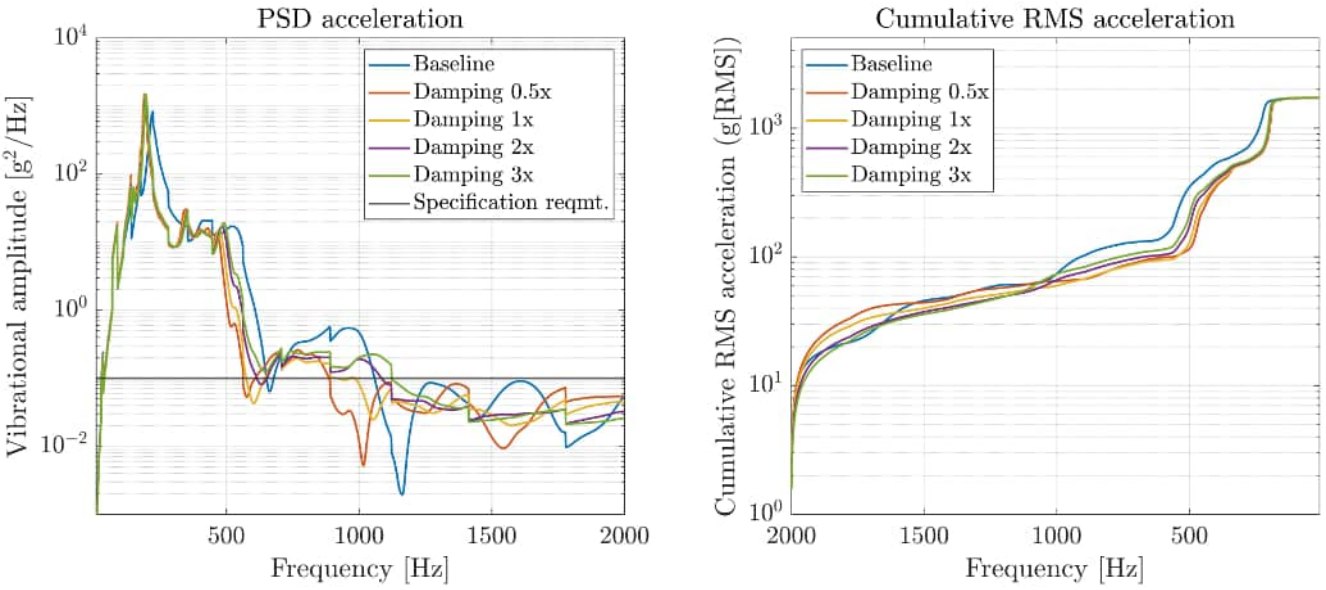

Figure 40: Results when varying Young's modulus and the loss factor for the damping mat rubber material. The left figure shows the PSD acceleration over the frequency span for a node at the middle of the downstream wall, on the reinforcement. The right figure shows the cumulative RMS acceleration with a flipped frequency axis, in which the cumulative sum starts from 2000 Hz and ends at 10 Hz.

Figure 40 shows how the PSD acceleration and RMS acceleration vary over the frequency span for a node in the middle of the downstream wall and the top row of the reinforcement, when varying the Young's modulus and loss factor. In the PSD plot, it is evident that below 200 Hz, the vibrational amplitude for all configurations is similar. However, the first eigenmode shifts to a lower frequency when damping mats are installed. Above 200 Hz, the vibrational amplitude for the baseline model is almost always higher than the configurations with damping mats installed. This result is also seen in the cumulative RMS acceleration plot, where the baseline model has a higher cumulative RMS acceleration than the other configurations between 200-1000 Hz. When analysing the four damping mat configurations, it is observed that they behave similarly in both the PSD and RMS plots. Comparing the baseline model against the damping mat configurations, it is clearly seen that the addition of added mass has shifted the peaks in the frequency span. This frequency shift is most clearly observed when comparing the weakest damping configuration (Damping 0.5x) at 1000 Hz to the baseline model at 1150 Hz.

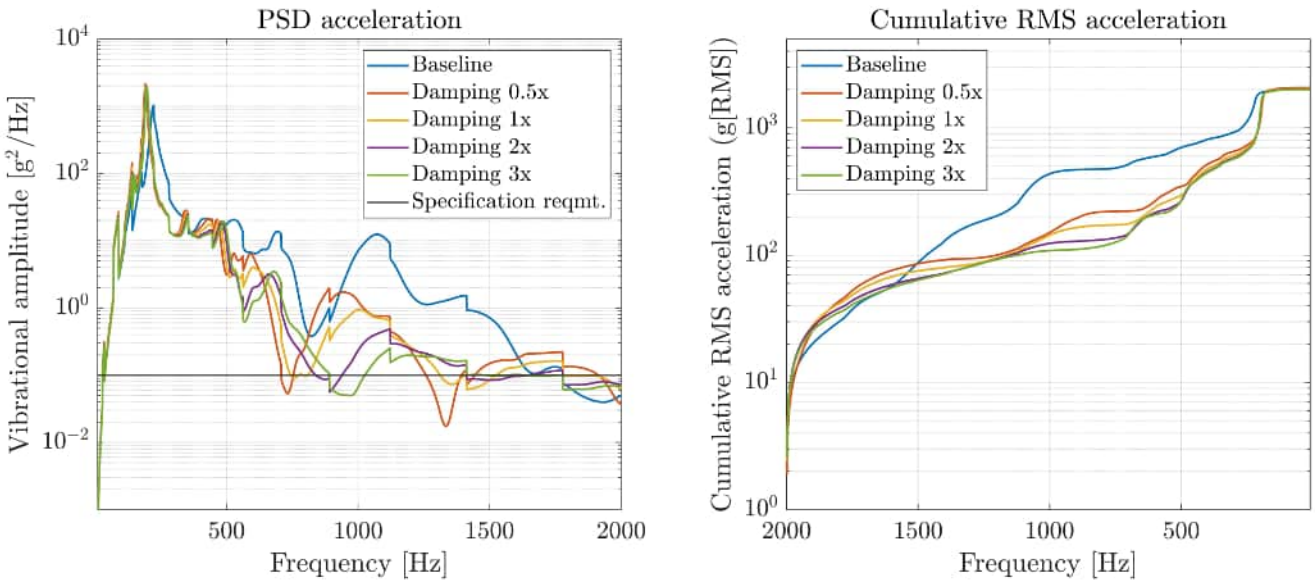

Figure 41: Results of varying Young's modulus and loss factor. The left figure shows the PSD acceleration across the frequency span for a node at the middle of the downstream wall, on the skin field. The right figure shows the cumulative RMS acceleration with the frequency axis flipped, where the cumulative sum starts at 2000 Hz and ends at 10 Hz.

Figure 41 illustrates how the PSD acceleration and RMS acceleration vary across the frequency span for a node located at the middle of the downstream wall, on the skin field. The differences between the configurations are more apparent than in Figure 40. When damping mats are installed, the first eigenmode of the downstream wall occurs at a lower frequency than when no damping mats are present. After the first eigenmode, the vibrational amplitude of the baseline model is generally higher than that of the two damping configurations, except above 1600 Hz. The skin field resonance is clearly visible in the cumulative RMS plot, where the cumulative RMS acceleration is significantly higher for the baseline model between 400-1600 Hz. This resonance is not an issue when damping mats are installed, indicating that the damping mats effectively dissipate the resonances.

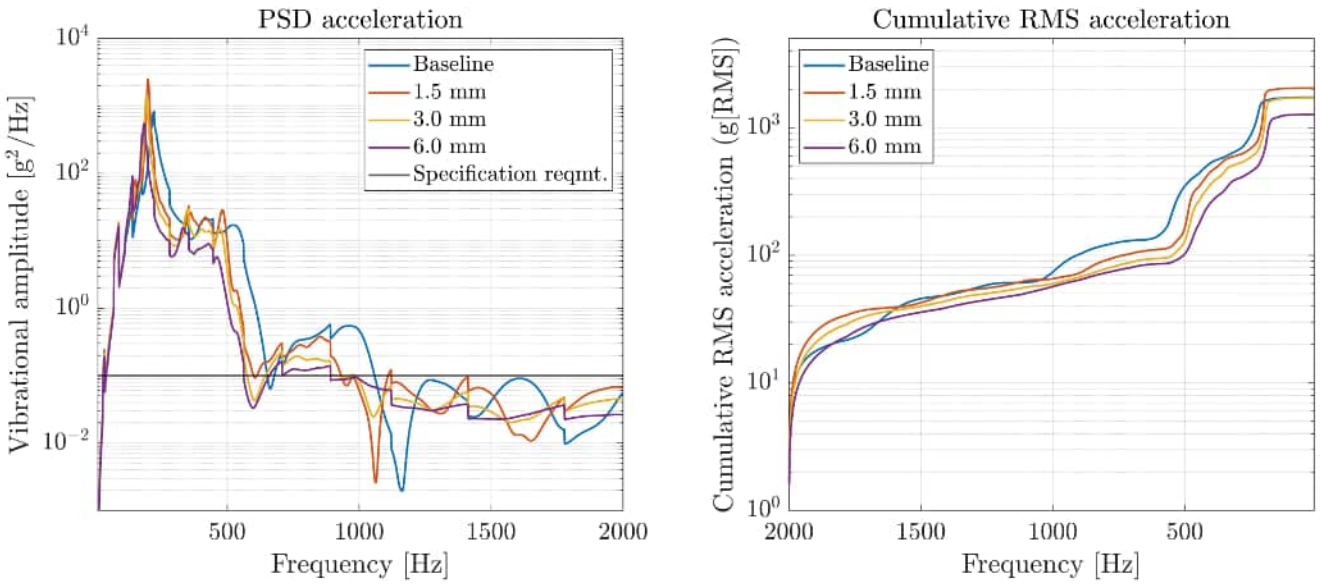

Figure 42: Results when varying the thickness of the rubber for the node on the reinforcement. Left figure shows the PSD acceleration over the frequency span. Right figure shows the cumulative RMS acceleration with flipped frequency axis in which the cumulative sum starts from 2000 Hz and ends at 10 Hz.

Figure 42 illustrates the PSD acceleration and RMS acceleration on the reinforcement for different configurations of rubber thickness configurations of damping mats. Notably, the addition of damping mats impacts the RMS acceleration, particularly between 200 and 1000 Hz, by reducing it compared to the baseline model. There is also a difference between the rubber-thickness configurations where an increased thickness correlates to a downward shift in the curve, indicating a reduction in vibrations. This displays the effectiveness of thicker rubber in mitigating vibrations.

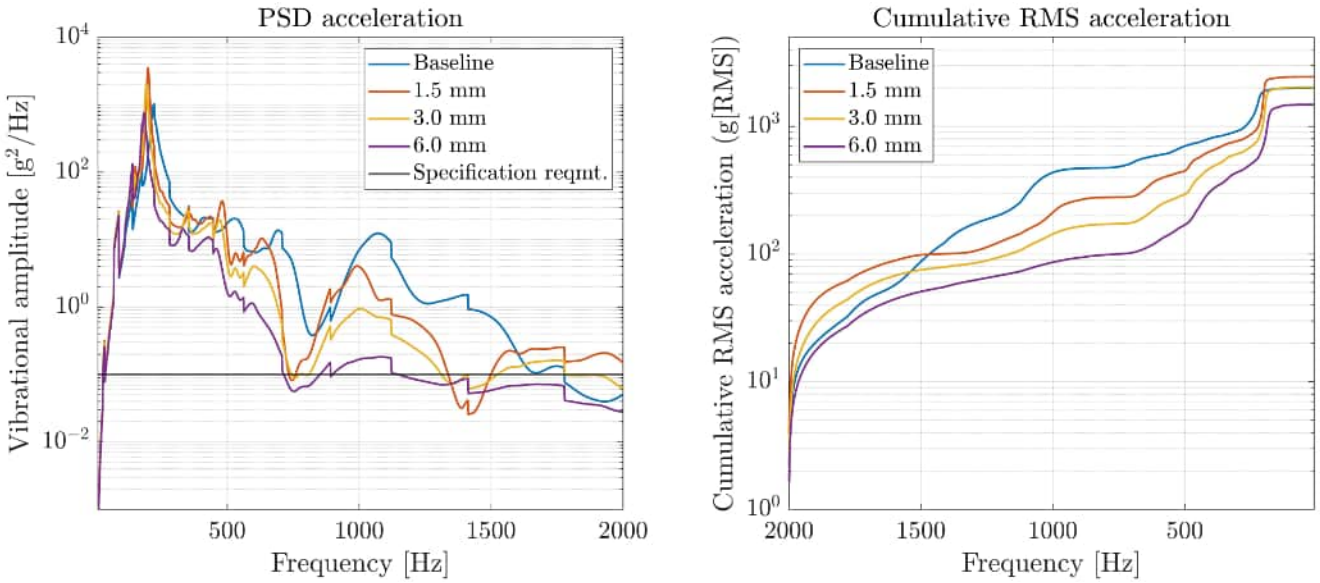

Figure 43: Results when varying the thickness of the rubber for the node on the skin field. Left figure shows the PSD acceleration over the frequency span. Right figure shows the cumulative RMS acceleration with flipped frequency axis in which the cumulative sum starts from 2000 Hz and ends at 10 Hz.

Figure 43 illustrates the PSD acceleration and RMS acceleration on the skin field for different configurations of rubber thickness for the damping mats. The results highlight distinct differences among the rubber configurations, particularly evident in the reduction of skin field resonance at 1100 Hz with increasing rubber thickness. This reduction significantly affects the RMS acceleration plot, showcasing improved vibration damping with thicker rubber. A rubber thickness of 6 mm is more effective at reducing vibrations over the whole frequency span compared to the other configurations. For lower frequencies a rubber thickness of 1.5 and 3 mm behave similar to the baseline model.

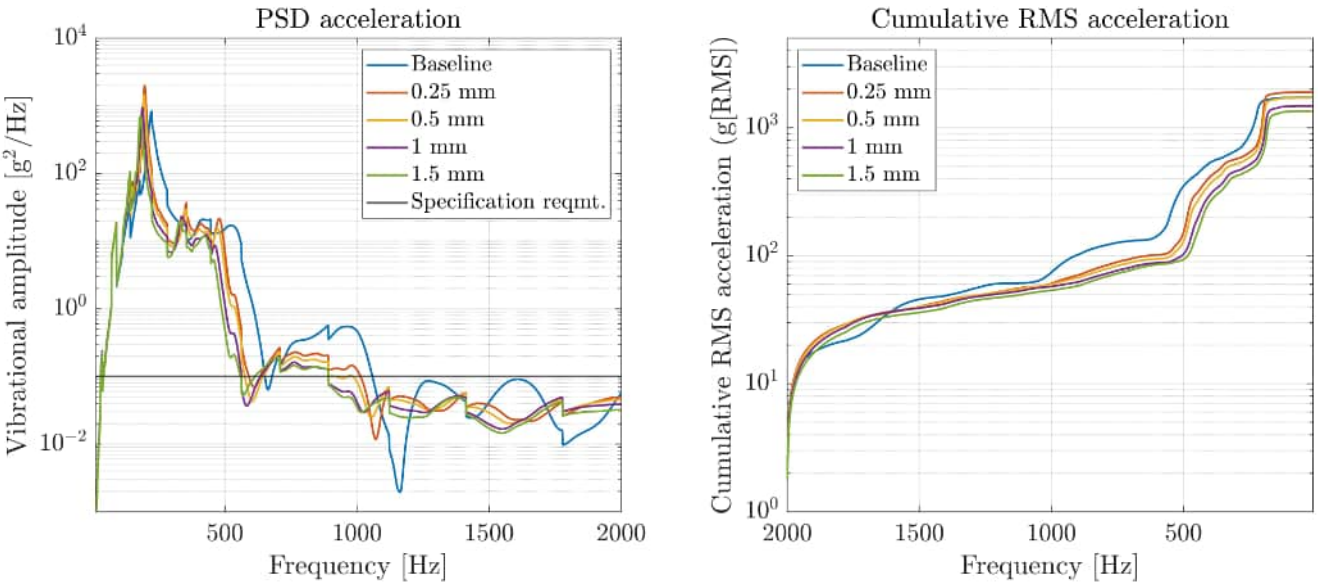

Figure 44: Results when varying the thickness of the aluminium panel for the node on the reinforcement. Left figure shows the PSD acceleration over the frequency span. Right figure shows the cumulative RMS acceleration with flipped frequency axis in which the cumulative sum starts from 2000 Hz and ends at 10 Hz.

Figure 44 shows the PSD acceleration and RMS acceleration on the reinforcement for different configurations of aluminium panel thickness attached to the damping mats.

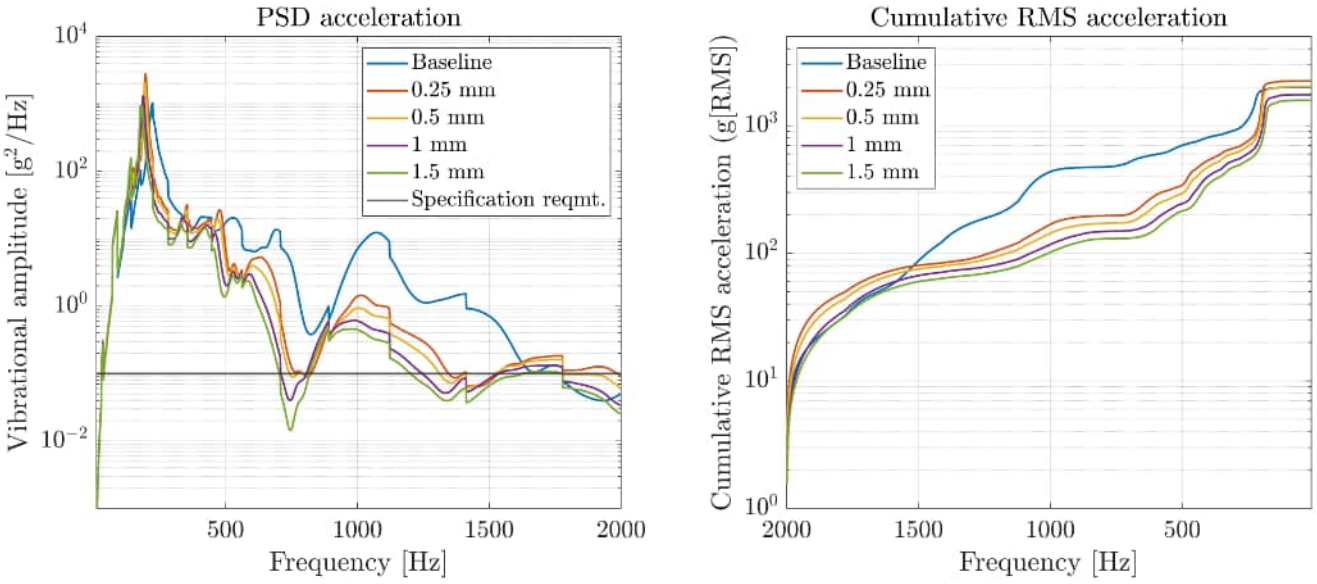

Figure 45: Results when varying the thickness of the aluminium panel for the node on the skin field. Left figure shows the PSD acceleration over the frequency span. Right figure shows the cumulative RMS acceleration with flipped frequency axis in which the cumulative sum starts from 2000 Hz and ends at 10 Hz.

Figure 45 shows the PSD acceleration and RMS acceleration on the skin field for different configurations of aluminium panel thickness for the damping mats. It can be seen that when the aluminium panel thickness increases, the PSD and RMS peak acceleration are offset to a lower frequency. The same result is seen in Figure 44 but the offset is smaller.

When comparing the results from Figures 40 to 45, it becomes evident that vibrational amplitudes are smaller on the reinforcement compared to the skin field. It is noted that damping mats reduce the vibrational amplitude more effectively on the skin field than on the reinforcement. It is thus an effective tool to reduce skin field resonance which generally appears between 200-1600 Hz. This suggests that equipment's should be mounted on the reinforcements. Between 1600-2000 Hz the baseline model seems to have a steep drop in acceleration compared to the damped cases.

The various parameters, including Young's modulus, the loss factor of the damping pad material, rubber thickness, and aluminium panel thickness, influence the amount of damping generated by the damping mats. Notably, in this model and load case, the thickness of the rubber and aluminium panel has a more significant impact on dissipating vibrational energy than changes in Young's modulus and loss factor. This finding is reasonable given the substantial difference in Young's modulus between the rubber material and aluminium.

When analysing the effect of the implementation of damping mats great care has to be taken regarding the impact on the natural frequency of the structure. The inclusion of damping, in the way modelled, affects the stiffness-to-mass ratio and thus the natural frequency. This becomes a problem when investigation the vibration propagation since at a specific frequency the response

will differ between the cases. Another issue that arises due to the shifting in natural frequency and is visible in the PSD acceleration plots in Figures 40-45is that the cases with damping applied generally leads to higher peak vibrational amplitude contrary to the theory where adding damping should decrease the peak amplitude. This however is due to how the excitation is implemented in one-third-octave bands. The shifting of natural frequency makes the excitation coincide with a higher magnitude step seen in Figure 28. Awareness must thus be taken when conducting a comparison between configurations in this way regarding the excitation and the one-third-octave band frequencies which it is given in.

Regarding the results when varying different parameters for the damping configuration it is visible that damping has an impact on the vibrational amplitude, as is most clear in the cumulative RMS acceleration plots in Figures 40-45. The vibrational amplitude in the skin field is also consistently more affected by the application of damping. All parameters investigated showed a trend of reducing vibrational amplitude with an increase in the parameter value. The parameters should however be seen in relation to each other to accurately tune the damping. The addition of damping mats do have an influence on the vibrational response of the structure and should therefore be modelled if a surface with damping mats in the aircraft is to be analysed regarding vibration.

4.4 Impact of equipment mounting position

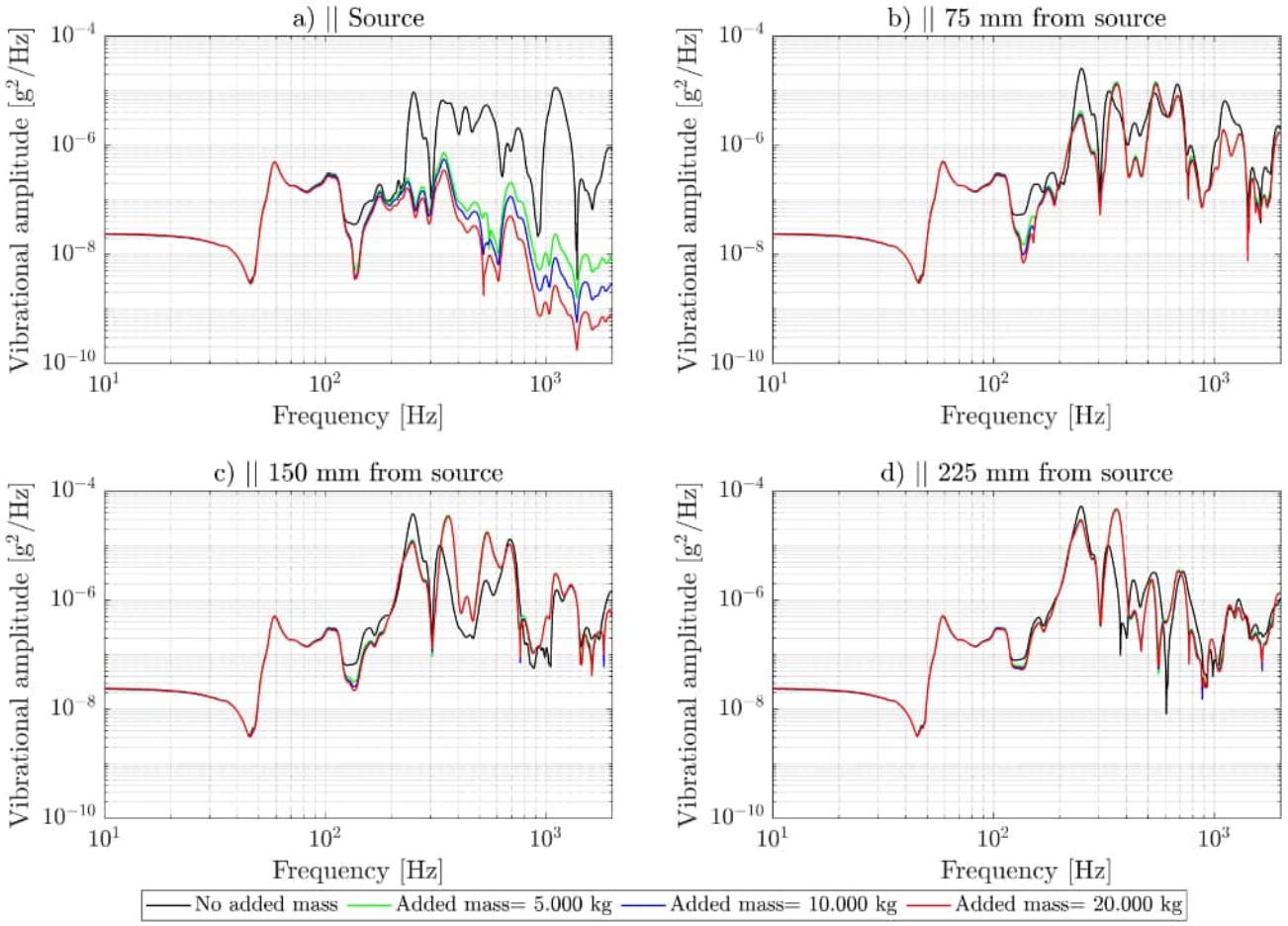

Figure 46: Showing results for response set 1 with mass added to mass point 2. Subplot a) shows the source which is the mass point while subplots b)-d) shows the response for an increase in distance from the source.

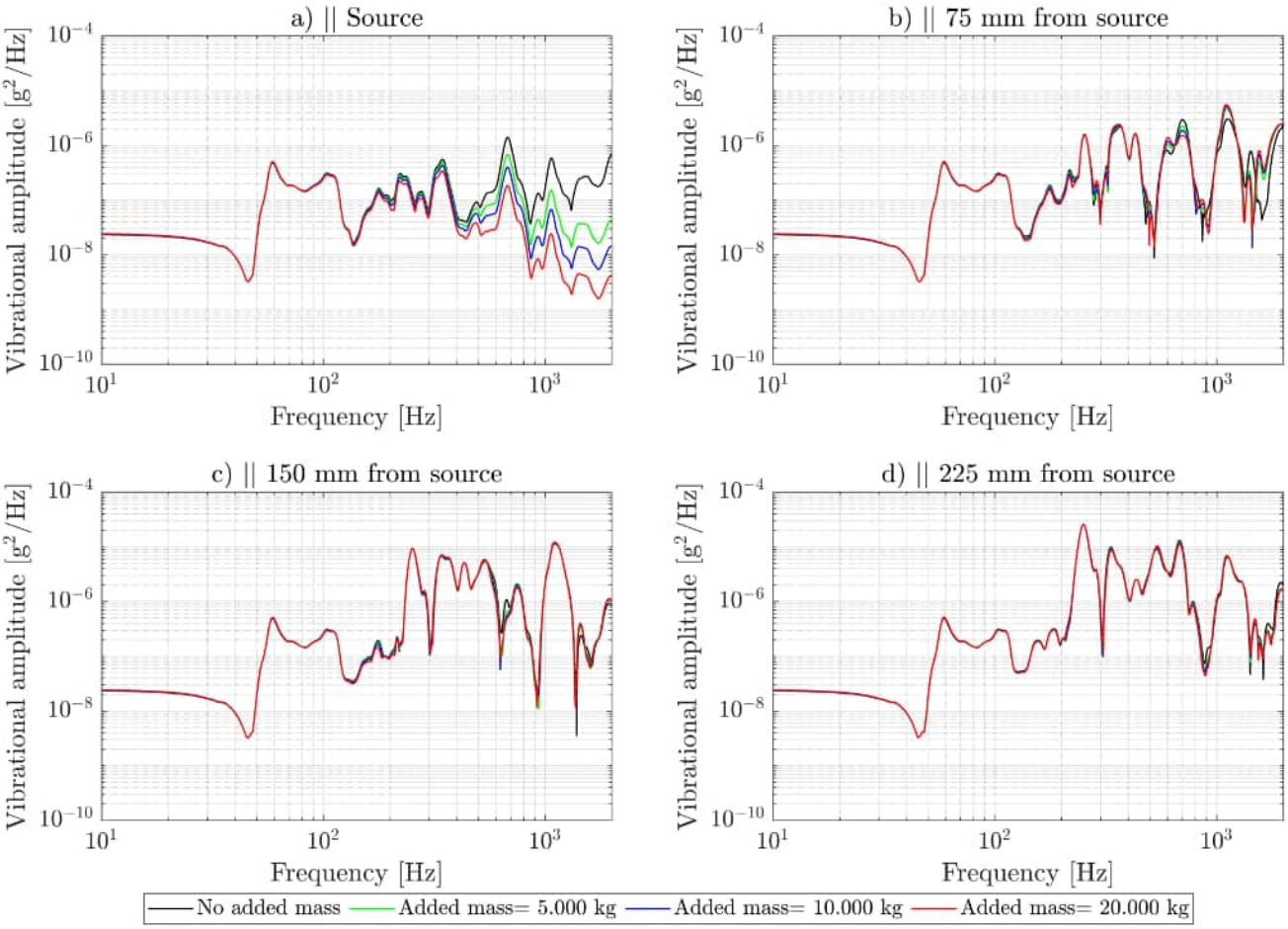

Figure 47: Showing results for response set 2 with mass added to mass point 1. Subplot a) shows the source which is the mass point while subplots b)-d) shows the response for an increase in distance from the source.

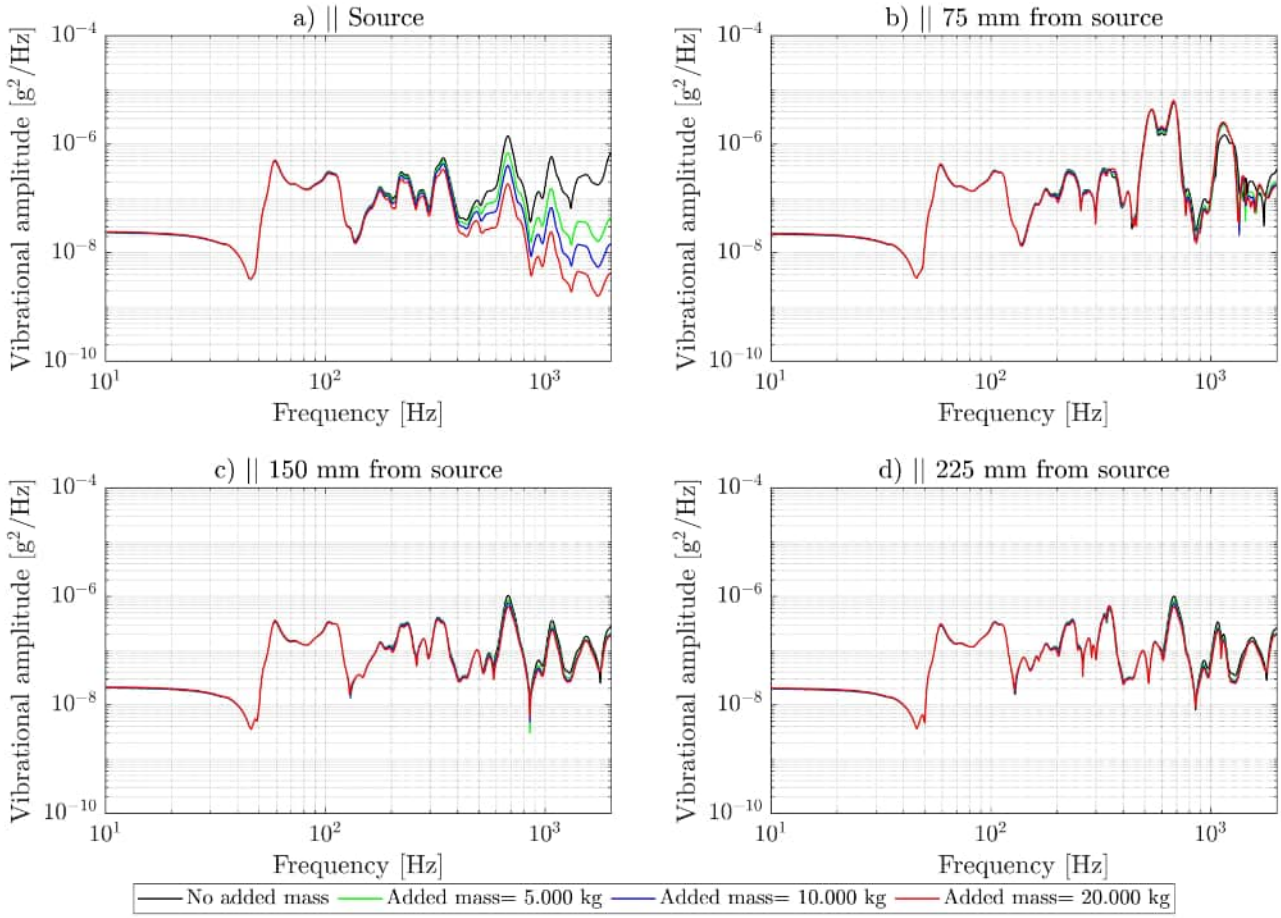

Figure 48: Showing results for response set 3 with mass added to mass point 1. Subplot a) shows the source which is the mass point while subplots b)-d) shows the response for an increase in distance from the source.

Figures 46a)-d), 47a)-d) and 48a)-d) displays the PSD acceleration in three different response sets, two different mass points and four different mass values. The results in all figures indicates that adding mass affects the vibrational response locally and for high frequencies. When examining the vibrational response at a distance from the source in Figure 46, it is observed that there are variations in vibrational amplitude further from the source, suggesting that the installation of equipment influences the vibrational response at locations distant from its installation. The same effect is not seen in Figures 47 and 48.

Comparing Figures 46 and 47 it is visible that the added mass have a much greater effect in mass point 1, especially in a) in the subplots. The case with no added mass have significantly higher amplitudes for higher frequencies for mass point 1. When adding mass however the PSD acceleration decreases at a higher rate. The two configurations have different configurations regarding the stiffness with mass point 2 being placed in a stiff connection while mass point 1 is placed more centrally on Frame 8, which could explain the slightly more oscillative behaviour of mass point 1 and the difference in impact of the mass.

Comparing Figures 47 and 48, both of which use mass point 2 as the applied mass, it is observable that they behave similarly. Some differences are noticeable depending on the distance from the source, likely due to local differences in stiffness between the two response sets. Overall, both sets exhibit the behaviour where the applied mass does not impact the PSD acceleration outside the source area.

Point masses are important to model due to the local effect on the dynamic behaviour it provides. The point masses considerably lowers the vibrational response locally and should be modelled to get an accurate dynamic behaviour. This is visible for frequencies above 500 Hz from Figures 46-48 subplot a). The mounting point of the mass also impacts the dynamic behaviour. From the result in Figure 37 subplot d)-f) where a point mass is passed and reduces the vibrational amplitude by a large degree locally, for higher frequencies. From subplot a) in the figure it is also visible that the black line is lower then the cyan coloured one. This indicates that the point mass effects the vibrational amplitude away from the source as well. The comparison between the equipment mounting and vibrational response cases is not entirely equitable, since the vibrational response case involves different connections through rigid body elements, other point masses, virtual fluid mass, and varying excitation, which could influence the result. Both cases however seem to indicate that the greatest effect is locally.

4.5 Validation

The vibration response levels obtained through the finite element model was compared with extrapolation curves from NASA Handbook 7005. An upper limit and a lower limit have been defined with a 6dB range to symbolise the crudeness of the predictions.

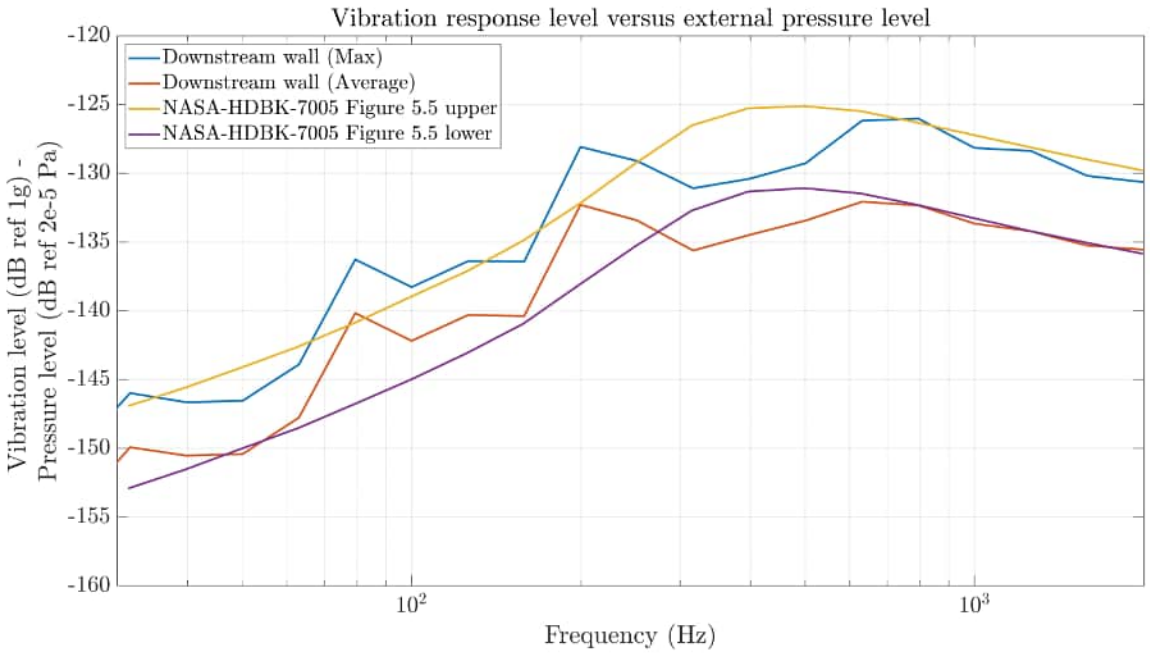

Figure 49: Comparison between extrapolation curve NASA-HDBK 7005 for the average and max values obtained at the downstream wall.

In Figure 49 the vibrational response minus the exterior pressure level has been plotted. The vibrational response was taken as an average of the downstream wall as well as its maximum value at each frequency step. The validation shows that methodology described in NASA-HDBK 7005 can be used to validate the downstream wall for an IWB in an aircraft model excited by sound pressure excitation.

The minimum value was not used in the validation due to the inconsistent stiffness in the connections compared to the rest of the downstream wall.

The validation of the results in this thesis is limited. The model has only been validated against one standard, which was an crude prediction derived from cylindrical space vehicles but demonstrated a strong correlation with the model.

5 Conclusion

Regarding the model fidelity the vibrations due to cavity oscillations will propagate outside of the IWB. The work conducted implicates that high model fidelity is required in the vicinity of the IWB. Analysing only the excitation due to flow over the open IWB the results indicate that equipment should not be placed in the vicinity of the downstream wall and IWB.

The model captures the dynamic behaviour well for the lower half of the frequency span. However, between 1000-1500 Hz, the resolution of wave propagation begins to diminish, and between 1500-2000 Hz, the mesh is inadequate. This issue arises due to the element size and order chosen for the analysis. To achieve accurate results for the upper half of the frequency span, smaller element sizes or higher-order elements should be used. For lower frequencies, the element sizes used in this model are sufficient to capture the wave propagation accurately.

Damping mats can be included and the existence of them decreases the vibrational response in the aircraft structure. How they are modelled have an impact on the vibrational response, where the investigated parameters showed a decreasing trend of the vibrational amplitude over the whole frequency span.

For the investigation into how the position of mounting equipment impact the vibrational response, further work need to be conducted to draw a more accurate conclusion. For the investigation performed, the addition of equipment seem to effect the vibrational response in the close vicinity of the mass with a decreasing effect further away from the source. The local behaviour of the mounting point regarding primarily stiffness influences which extent the mass impacts the vibrational response. In a mass point with high local structural stiffness the mass has less impact compared to a mass point with lower local structural stiffness.

6 Further work

To predict the dynamic behaviour of the structure and equipment vibration environment at an open IWB during supersonic flight, this work shows the need to include detailed description of the load, the modelling of the structure and evaluation of stresses of the structure as well as the vibration environment of the equipment. All these areas needs to be further developed.

For the excitation by the open cavity flow, this work only focuses on known standards so the next step is to apply CFD simulations to try and get a more realistic excitation on the IWB.

The level of detail in the CAD geometry and generated finite element model needs to be enhanced to predict the vibration response and propagation. For example, the description of the the structural components how they are are joined together are here very simplified.

The evaluation procedures both for stress analysis and for the vibration environment needs further development.

With improved level of detail, it will be interesting to analyse how the vibration response is affected by varying the cavity geometry and when introducing measures to reduce the dynamic pressure and vibration response.

References

[1] Saab, "Company in breif." https://www.saab.com/about/company-in-brief. [accessed: 18.01.2024].

[2] Saab, "Organisation." https://www.saab.com/about/company-in-brief/organisation. [accessed: 18.01.2024].

[3] S. Nilsson, *Advanced Fluid-Structure Interaction Modelling and Simulation for Aerospace Applications*. Licentiate thesis, Chalmers University of Technology, Gothenburg, Sweden, 2022.

[4] C. B. Chinoy, "ESDU18011-Cavity oscillations," 2019.

[5] B. Outten, M. Sheehan, Y. Mehta, and R. Kumar, "Effect of door angle and leading wedge on the cavity acoustics at supersonic speeds," (Chicago and online), AIAA AVIATION 2022 Forum, June-July 2022.

[6] A. T. Amour, D. S. Crowe, and B. A. Jolly, "The effect of stores on cavity acoustics," (Chicago and online), AIAA AVIATION 2022 Forum, June-July 2022.

[7] C. W. de Silva, *Vibration fundamentals and practice*. CRC Press, 2006.

[8] P. H. Wirsching, T. L. Paez, and K. Ortiz, *Random Vibrations. Theory and Practice*. John Wiley & Sons, Inc, 1995.

[9] P. Stoica and R. Moses, *Spectral Analysis of Signals*. Prentice Hall, Inc, 2005.

[10] D. J. Inman, *Engineering Vibrations*. Pearson Education Limited, 4 ed., 2014.

[11] Autodesk, "Section 24: Frequency response analysis." https://help.autodesk.com/view/NINCAD/2022/ENU/?guid=GUID-FCA4E4B5-1A53-480E-A43A-A208E8F3C97E. [accessed: 19.03.2024].

[12] C. W. de Silva, *Vibration Damping, Control, and Design*. Boca Raton : Taylor & Francis, 2007.

[13] GMT-Rubber, "Using rubber for effective anti vibration." https://www.gmtrubber.com/using-rubber-effective-anti-vibration/. [accessed: 16.04.2024].

[14] Engineering Science Data Unit, "ESDU.E.07.01-Endurance of aluminium alloys (unclad) (in bending)," 1993.

[15] A. D. Nashif, D. I. G. Jones, and J. P. Henderson, *Vibration damping*. John Wiley & Sons, 1985.

[16] X. Song, "Optistruct random response analysis," 2023.

[17] Altair, "1d elements." https://2021.help.altair.com/2021/hwdesktop/hwx/topics/pre_processing/entities/elements_1d_r.htm, 2021. [accessed: 10.05.2024].

[18] Altair, "Elements." https://2021.help.altair.com/2021/hwdesktop/hm/topics/pre_processing/entities/elements_r.htm?zoom_highlightsub=bar2. [accessed: 19.03.2024].

[19] Altair, "Shell elements." https://2022.help.altair.com/2022.2/hwsolvers/rad/topics/solvers/rad/shell_elements_c.htm, 2022. [accessed: 10.05.2024].

[20] B. Webster, "First-order vs. second-order elements in fea." https://www.fidelisfea.com/post/first-order-vs-second-order-elements-in-fea, 2021. [accessed: 10.05.2024].

[21] Altair, "Cquad4." https://2021.help.altair.com/2021/hwsolvers/os/topics/solvers/os/cquad4_bulk_r.htm, 2021. [accessed: 10.05.2024].

[22] Grasp-Engineering, "Different types of fea elements / how to decide the element type." https://www.graspengineering.com/different-types-of-fea-elements-how-to-decide-the-element-type/. [accessed: 13.05.2024].

[23] Autodesk, "Degrees of freedom." https://help.autodesk.com/view/NINCAD/2024/ENU/?guid=GUID-8DDFF3C1-5EBB-4146-85DD-8D54F311C4B5. [accessed: 13.05.2024].

A Random Response analysis

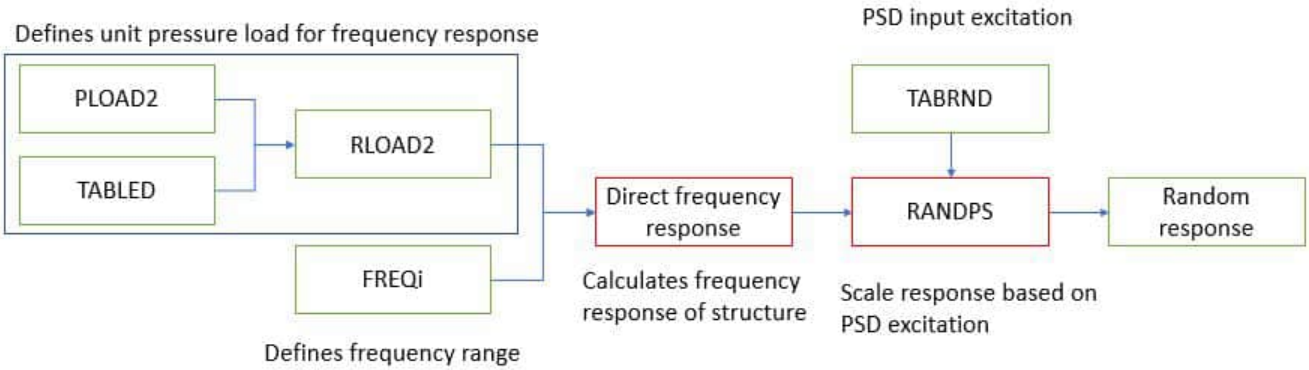

Figure 50: Flowchart detailing the random response process in OptiStruct.

Figure 50 shows how a random response analysis is solved in OptiStruct. Both input excitation and random respons is defined by a PSD. [16]

B Fundamental Finite elements

B.1 1D elements

1D elements are used when analysing line-type structures where one dimension is much larger than the other two dimensions. The shape of a 1D element is a line with the cross sectional area assigned to the element as input. 1D elements are computationally very cheap compared to modelling as a 2D or a solid element.

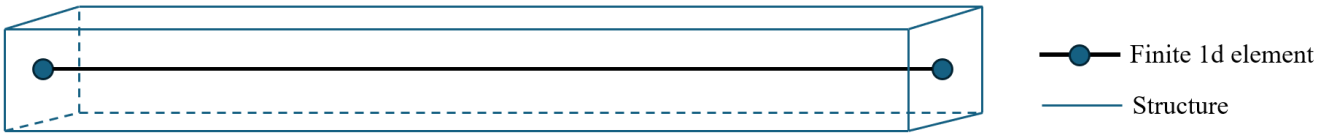

Figure 51: 1D element compared to a 3D structure.

Figure 51 shows the relation between a 1D element and a 3D structure. The 1D element is defined in the middle of the structure.

Figure 52: Difference between a first- and second order 1D element.

Figure 52 shows the difference between a first- and second order 1D element.Second order 1D element has a node in the middle of the element meaning that the element can curve. A first order

1D element is unable to curve making it linear. Using second order 1D element leads to a more accurate solution at the cost of computational time. Both first- and second order 1D elements found in Hypermesh are used to model axial, bending, and torsion behaviour. [17]

B.1.1 bar2 elements

The formulation chosen to model the stiffened plates using 1D elements in OptiStruct was the bar2 element. The bar2 element is a first-order element with two nodes, offering a computationally effective solution while encompassing axial, bending, and torsion behaviour. [18]

B.2 Shell elements

Shell elements are among the most commonly used elements in finite element analysis (FEA). They are especially suitable for structures where one dimension, typically the thickness, is much smaller than the other two. Utilizing shell elements simplifies the modelling of thin-walled structures like aircraft fuselages by reducing three-dimensional complexities into two-dimensional representations. By abstracting these structures into shell elements, the number of nodes and elements are reduced. This reduction leads to a decrease in computational time and resources, making shell elements a highly efficient choice for analysing large, complex assemblies with thin geometries. [19]

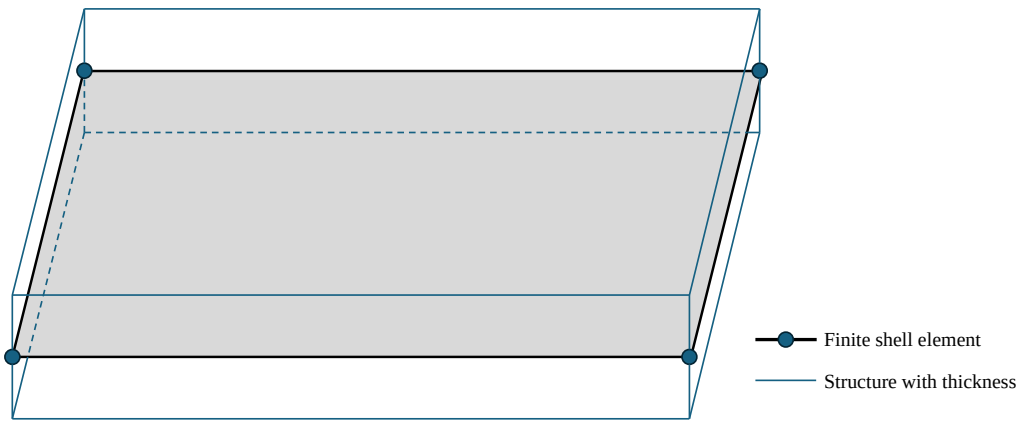

Figure 53: A shell element and how it relates to a structure with thickness.

Figure 53 illustrates a shell element and how it relates to a structure with thickness. The shell element is defined at the mid-surface plane of the structure. A shell element can be either quadratic or triangular with different number of nodes in each element. Figure 53 shows a QUAD4-element meaning it is quadratic and have four nodes in each element. [19]

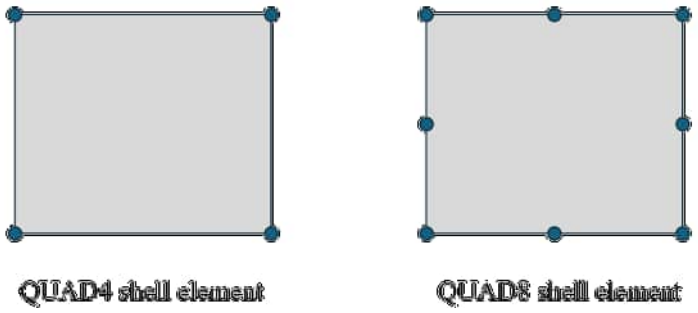

Figure 54: Difference in nodes between the QUAD4- and QUAD8-shell-element.

Figure 54 demonstrates a QUAD4- and a QUAD8-element. As seen, a QUAD4-element has four nodes while a QUAD8-element has eight nodes. Since nodes are located on the middle of each edge in a QUAD8-element, it allows for curved edges of each element. Due to this feature, QUAD8-elements are referred to as quadratic second-order elements. QUAD4-elements, being unable to have curved edges, only allow curvature to be approximated by segmenting the edge into straight lines across multiple elements. This makes them linear first-order elements. This leads to QUAD8-elements giving a more accurate solution at a cost of computational time. [20]

The shell element used in Hypermesh has six dofs meaning each node allows translation and rotation along all axes. It can thus capture both membrane stresses and bending stresses. [21]

B.3 Solid elements

Solid elements are three-dimensional volumetric entities in 3D space. These elements are applicable when all dimensions are of similar magnitude. Various shapes of solid elements exist, including hexahedrons, tetrahedrons, prisms, and pyramids. They are chosen based on specific conditions. Tetrahedrons are for instance suitable for complex geometrical shapes, whereas hexahedrons are preferred for models with rectangular configurations. [22]

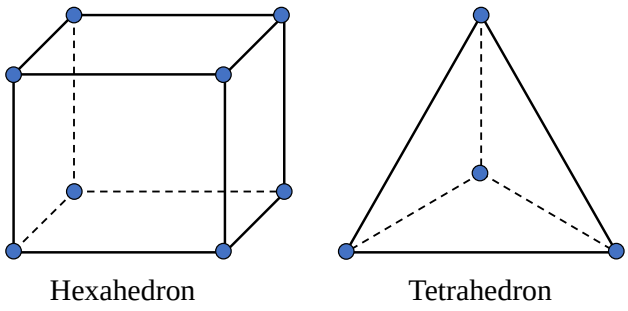

Figure 55: Difference in nodes between a hexahedron and tetrahedron first order element.

Figure 55 illustrates the distinctions between first order hexahedral (HEX8) and tetrahedral (TETRA4) elements. In second order solid elements, nodes are positioned at the midpoints of each edge, enabling the elements to have curved edges. The adoption of second order elements increases accuracy but also increases computational time due to the higher number of nodes. [22]

A solid element has three dofs per node meaning that a first order hexahedric element has 24 dofs. Solid elements only supports translational dofs thus moments can not be directly applied to solid elements. [23]

B.4 CONM2 elements

The mass element used to model concentrated points of mass in the model is the CONM2 formulation in optistruct. This formulation allows for accurate modelling of discrete masses, such as components or payloads, within the finite element analysis. [18]

B.5 RBE3 elements

The RBE3 element serves to model a distributed connection between the CONM2 mass element and the surrounding nodes in the finite element analysis. Unlike elements that alter the stiffness of the model, RBE3 is designed to maintain the integrity of the stiffness. This is achieved by designating one dependent node, in this case the CONM2 element's node, and multiple independent nodes. The motion of the dependent node is then determined as the average of the motion of the independent nodes. Consequently, the load from the mass is distributed among the independent nodes, accounting for their local stiffness characteristics without altering the overall stiffness of the model. [18]

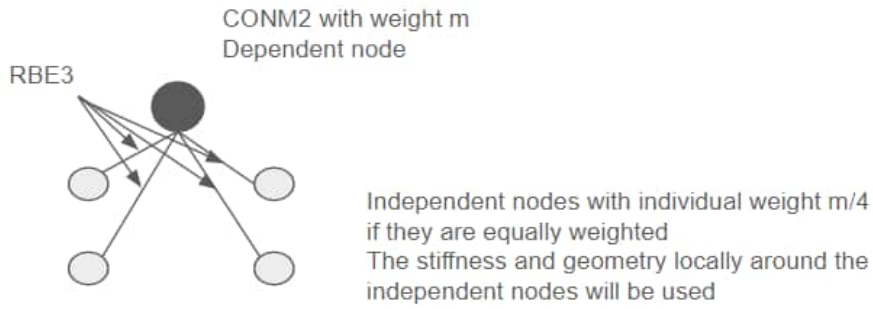

Figure 56: Visualisation of how the RBE3 element divides mass.

Figure 56 shows how the connection between the dependent and independent node works. The dependent node is the black node in the figure and the four white nodes are the independent nodes.

B.6 MFLUID

B.6.1 Theory and Method

In the dynamic analysis of aircraft structures, it is essential to account for the presence of fuel, which introduces fluid mass effects. To address this, a virtual fluid mass approach was employed using the MFLUID card within OptiStruct. Unlike traditional methods that require explicit modelling of the fluid volume, the MFLUID card offers a simplified solution. By incorporating virtual fluid masses, the structural model can accurately capture the effects of fluid mass without the need for meshing, by influencing the mass and inertia. Moreover, this approach ensures a comprehensive coupling between acceleration and pressure at the fluid-structure interface. [18]

The fluid modes can be calculated in two different ways, VMOPT 1 and VMOPT 2. VMOPT 1 uses the virtual fluid mass and puts it into the mass matrix for the analysis, while VMOPT 2 calculated the dry modes of the structure and then approximates the wet modes. VMOPT 2 has a slight loss of accuracy compared to VMOPT 1 but reduces the computational time. For VMOPT 2 to produce accurate results the number of dry modes should be 2-4 times higher than the number of wet modes. Because the direct frequency response method was chosen, VMOPT 1 had to be selected. VMOPT 2 can only be selected if the modal frequency response method was chosen.

First, a local coordinate system is defined on the floor of the aircraft with the local z-axis pointing downwards. Then, 12 surface sets are created to contain the fuel. The surface sets consists of the side wall IWB and the connecting floor. The surface sets are visible in Figure 19.

The boxes are then filled by defining a free surface height for the fuel. The distance between the floor and the lowest part of the box is 600 mm. Therefore, a free surface height of 601 mm is chosen to ensure that the entire box is filled.

B.6.2 Comparison with and without MFLUID

The implementation of fuel was compared with a configuration consisting of CONM2 with RBE3 elements. The CONM2 elements were attached with RBE3 elements in the same area as where the virtual fluid mass was applied and acted in the same direction as the fluid mass. So in this case the models have identical mass in all directions.

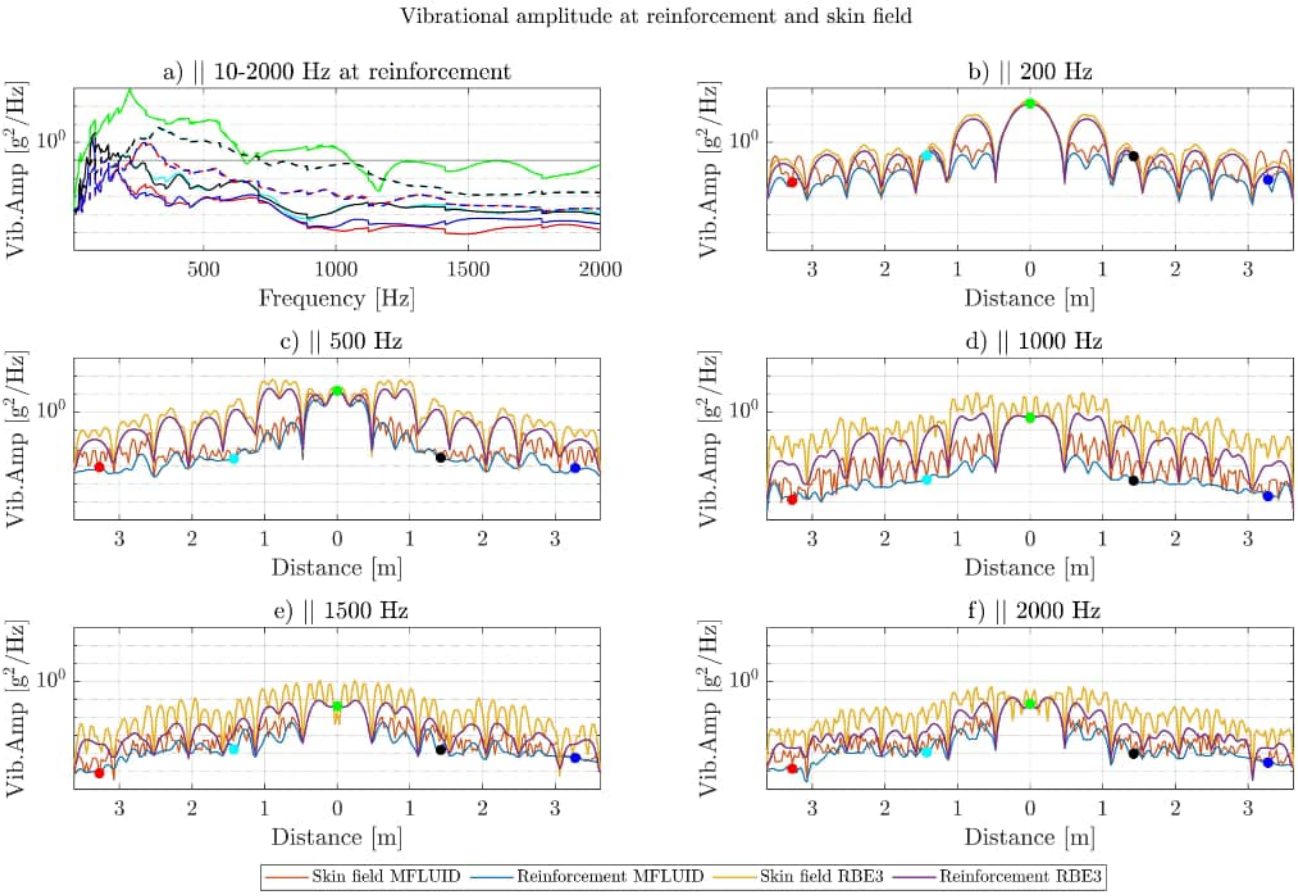

Figure 57: Comparison between MFLUID and RBE3 elements for node set 4. Subplot a) displays the vibrational amplitude over the frequency span. The dotted lines are the result using RBE3 elements and the solid line represents the result using MFLUID. The lines with the same colour represents the results from the same node for the two configurations. Subplots b)-f) shows the vibration propagation for a given frequency.

The effects of MFLUID is visible in Figure 57 and highlights the effect of coupling between the fluid structure interface that virtual fluid mass provides. It can be noted that RBE3 leads to a higher vibrational amplitude for all frequencies compared to MFLUID, especially visible for the lower frequencies.